JGR Atmospheres

RESEARCH ARTICLE
10.1029/2023JD040544

Special Collection:
The Arctic: An AGU Joint Special Collection

Measured and Modeled Trends of Seven Tropospheric Pollutants in the High Arctic From 1999 to 2022

T. Wizenberg[1], K. Strong[1], D. B. A. Jones[1], J. W. Hannigan[2], I. Ortega[2], and E. Mahieu[3]

[1]Department of Physics, University of Toronto, Toronto, ON, Canada, [2]National Center for Atmospheric Research, Boulder, CO, USA, [3]Institute of Astrophysics and Geophysics, UR SPHERES, Université de Liège, Liège, Belgium

Key Points:

- Consistent seasonal cycles were observed for seven tropospheric pollutants from the measurements of two high Arctic ground-based FTIRs
- CO, C_2H_2, and CH_3OH showed clear negative trends in the Arctic, while C_2H_6 and PAN displayed positive trends
- GEOS-Chem High Performance reproduced the observed trends of CO, C_2H_2, and CH_3OH, but showed differing trends for C_2H_6, H_2CO, and PAN

Supporting Information:

Supporting Information may be found in the online version of this article.

Correspondence to:

T. Wizenberg,
wizenberg@atmosp.physics.utoronto.ca

Citation:

Wizenberg, T., Strong, K., Jones, D. B. A., Hannigan, J. W., Ortega, I., & Mahieu, E. (2024). Measured and modeled trends of seven tropospheric pollutants in the high Arctic from 1999 to 2022. *Journal of Geophysical Research: Atmospheres*, *129*, e2023JD040544. https://doi.org/10.1029/2023JD040544

Received 22 DEC 2023
Accepted 1 JUN 2024

Author Contributions:

Conceptualization: T. Wizenberg, K. Strong, D. B. A. Jones
Data curation: T. Wizenberg, K. Strong, J. W. Hannigan, I. Ortega, E. Mahieu
Formal analysis: T. Wizenberg
Funding acquisition: K. Strong
Investigation: T. Wizenberg, D. B. A. Jones, I. Ortega, E. Mahieu

Abstract The long-term trends and seasonality of many tropospheric pollutants are not well characterized in the high Arctic due to a dearth of trace-gas measurements in this remote region. In this study, the inter- and intra-annual variabilities of carbon monoxide (CO), acetylene (C_2H_2), ethane (C_2H_6), methanol (CH_3OH), formaldehyde (H_2CO), formic acid (HCOOH), and peroxyacetyl nitrate (PAN) in the high Arctic region were derived from the total column time-series of ground-based Fourier transform infrared (FTIR) measurements at Eureka, Nunavut (80.05°N, 86.42°W, 2006–2020) and Thule, Greenland (76.53°N, 68.74°W, 1999–2022). Consistent seasonal cycles were observed in the FTIR measurements at both sites for all species. Negative trends were observed for CO, C_2H_2, and CH_3OH at both sites, and for HCOOH at Eureka. Positive trends were detected for C_2H_6 and H_2CO at both sites, and for PAN at Eureka. Additionally, a 19-year simulation was performed using the novel GEOS-Chem High Performance model v14.1.1 for the period of 2003–2021. The model was able to reproduce the observed seasonality of all gases, but all species showed negative biases relative to observations, and CH_3OH was found to have a particularly large bias of approximately −70% relative to the FTIR measurements. The GEOS-Chem modeled trends broadly agreed with observations for all species except C_2H_6, H_2CO, and PAN, which were found to have opposite trends in the model. For some species, the measurement-model differences are suspected to be the result of errors or underestimations in the emissions inventories used in the simulation.

Plain Language Summary In this study, we investigate the seasonality and long-term trends of seven atmospheric pollutants measured from ground-based spectrometers at two locations in the North American high Arctic; Eureka, Nunavut (80.05°N, 86.42°W, 2006–2020), and Thule, Greenland (76.53°N, 68.74°W, 1999–2022). We observe consistent seasonal cycles at both sites for all gases. Carbon monoxide and acetylene were found to be decreasing over the years at both locations, while others gases, like ethane and formaldehyde were steadily increasing. At Eureka, formic acid concentrations were also found to be steadily decreasing. To better understand these changes, we used a chemical transport model to simulate the behavior of these gases in the high Arctic over a 19-year period (2003–2021). The model broadly captured the shape of the seasonal cycles, however, the simulation displayed some discrepancies relative to the ground-based measurements. For some gases, such as methanol and peroxyacetyl nitrate, the model showed greater discrepancies with the measurements than for others. The model reproduced the observed trends for all species except ethane, formaldehyde, and peroxyacetyl nitrate, which were found to have opposite trends in the model. Some of these discrepancies are believed to be attributed to errors in the model's emissions inventories.

1. Introduction

The Arctic region is a major receptor of transported mid-latitude pollution, and it is highly sensitive to changes in atmospheric composition (Law & Stohl, 2007; Stohl, 2006). Future anthropogenic climate change is expected to influence the Arctic troposphere by altering the transport pathways of pollutants, and by modulating the strength of emissions sources (Flannigan et al., 2005; Kirchmeier-Young et al., 2019; Shindell et al., 2006, 2008). Furthermore, reductions in summer sea ice coverage in recent years have accelerated the pace of industrialization in the Arctic and local emissions from mining, shipping, fossil fuel extraction, and infrastructure development have already been found to have a growing impact on the Arctic atmosphere (Marelle et al., 2016; Roiger et al., 2015). Wildfires have also been found to present a significant periodic source of air pollution to the Arctic, and they can contribute significant quantities of both aerosols and reactive trace gases to the region (Lutsch et al., 2016, 2019, 2020; Roiger et al., 2011; Viatte et al., 2013, 2014, 2015; Wizenberg, Strong, Jones, Lutsch, et al., 2023). Reactive tropospheric pollutants including volatile organic compounds (VOCs) can have various

Methodology: T. Wizenberg, K. Strong, D. B. A. Jones
Project administration: K. Strong, D. B. A. Jones
Resources: T. Wizenberg, D. B. A. Jones, J. W. Hannigan, I. Ortega, E. Mahieu
Software: T. Wizenberg
Supervision: K. Strong, D. B. A. Jones
Validation: T. Wizenberg
Writing – original draft: T. Wizenberg
Writing – review & editing: T. Wizenberg, K. Strong, D. B. A. Jones, J. W. Hannigan, I. Ortega, E. Mahieu

negative impacts on the Arctic climate and environment, which include enhancing warming in the region, the acidification of soil and rainwater, and contributing to poor air quality episodes (Galloway et al., 1982; Law & Stohl, 2007; Law et al., 2014; Shindell & Faluvegi, 2009; Whaley et al., 2022).

Monitoring and assessing the inter- and intra-annual variability of tropospheric pollutants in the high-Arctic region is challenging due to the scarcity of reliable long-term measurements. As a result, the budgets, seasonal cycles, and trends of many reactive tropospheric trace gases, including the contributions of biomass burning, are currently not well quantified in the Arctic. In the past, efforts to measure tropospheric pollution in the Arctic were largely carried out on a short-term campaign basis, and it is difficult to extrapolate information on intra- and inter-annual variability from these temporally limited measurements (e.g., Alvarado et al., 2010; Law et al., 2014; Liang et al., 2011; Singh et al., 1992; Wofsy et al., 1992). Satellite observations of many reactive tropospheric pollutant species have been made from sensors such as the Measurements of Pollution in The Troposphere (MOPITT; e.g., Deeter et al., 2003), the Tropospheric Emission Spectrometer (TES; e.g., Cady-Pereira et al., 2012, 2014; Payne et al., 2014), the Infrared Atmospheric Sounding Interferometer (IASI; e.g., Coheur et al., 2009; Franco et al., 2021; Pommier et al., 2016; Razavi et al., 2011), and the Cross-track Infrared Sounder (CrIS; e.g., Payne et al., 2022; Shogrin et al., 2023). However, the observational conditions for thermal infrared nadir-sounding instruments in the high Arctic are generally poor due to low thermal contrast and relatively low ambient concentrations of many pollutants, leading to higher uncertainties and sparser measurements than at lower latitudes. To this end, ground-based Fourier transform infrared (FTIR) spectroscopy is a valuable tool for studies of reactive tropospheric pollutants in the high Arctic as these instruments provide a consistent data set at a specific site, and generally possess greater vertical sensitivity and lower detection limits than nadir-viewing satellite instruments, particularly where low thermal contrast presents significant challenges for space-based infrared measurements.

In addition to ground- and space-based observations, global chemical transport models (CTMs) such as GEOS-Chem (http://geos-chem.org) can provide another valuable perspective on the transport, chemistry, and trends of these tropospheric pollutants, providing information where there are sparse or no measurements available. However, the high Arctic is a notoriously difficult region to simulate with CTMs due to the extreme atmospheric and solar conditions, poorly constrained local sources and sinks, and the occurrence of transport errors due the presence of model grid singularities at the poles leading to discrepancies across models (Shindell et al., 2008; Stohl et al., 2013; H. Yang et al., 2020; Yu et al., 2018). As a result, it is crucial to evaluate the performance of CTMs in remote regions such as the high Arctic, which are not often the focus of model validation exercises.

In this study, we assess the seasonal variability and long-term trends of carbon monoxide (CO), acetylene (C_2H_2), ethane (C_2H_6), methanol (CH_3OH), formaldehyde (H_2CO), formic acid (HCOOH), and peroxyacetyl nitrate (PAN) in the high Arctic region from the total column time-series measured by ground-based FTIRs at two sites; Eureka, Nunavut, Canada, and Thule, Greenland. Additionally, we perform a 19-year simulation using the novel GEOS-Chem High Performance (GCHP) CTM which covers the period of 2003–2021. We examine the modeled seasonal and inter-annual variability of these seven tropospheric trace gas species, and we evaluate the performance of the model against the ground-based FTIR observations at the two high-Arctic sites.

This paper is structured as follows. The ground-based FTIR measurement sites, instruments, and retrieval methods are described in Section 2.1. The GEOS-Chem model configuration and simulation used in this study are described in Section 2.2. The methodology used for estimating trends from the measured and modeled data are discussed in Section 2.3. In Section 3.1, the seasonal cycles obtained from the ground-based FTIR data at Eureka and Thule are presented, while in Section 3.2 the observed long-term trends derived from the FTIR measurements are discussed. In Section 3.3, the GEOS-Chem simulated seasonal cycles and trends are presented, and they are contrasted with the observational results. Conclusions are presented in Section 4.

2. Data and Methods

2.1. Ground-Based FTIR Measurements

2.1.1. FTIR Sites

In this study, measurements from two high-Arctic ground-based FTIRs were used. The first instrument is located at the Polar Environment Atmospheric Research Laboratory (PEARL) in Eureka, Nunavut (80.05°N, 86.42°W, 610 m a.s.l) on Ellesmere Island in the Canadian Arctic. The instrument is a Bruker IFS 125HR FTIR

spectrometer, and was installed at PEARL in July 2006. Measurements are made during sunlit clear-sky conditions using a custom-built heliostat. At present, the time-series of PEARL-FTIR measurements extends from August 2006 until March 2020, when the COVID-19 pandemic halted nominal operations. A detailed description of the Eureka FTIR is provided in Batchelor et al. (2009).

The second ground-based instrument is located at the Thule Airforce Base (TAB) in Thule, Greenland (76.53°N, 68.74°W, 225 m a.s.l.). A Bruker IFS 120M FTIR was installed at TAB in mid 1999, with measurements beginning in Fall 1999. The Thule FTIR is also equipped with a computer-controlled heliostat, and an automated liquid nitrogen fill-system to cool the detectors, allowing the instrument to be operated semi-autonomously. In 2015, the Bruker IFS 120M was replaced by a Bruker IFS 125HR, and an improved heliostat system was also installed. The time-series of Thule FTIR measurements covers the period of October 1999 to October 2022, although some trace-gas species are not retrieved over the full time-series. A detailed description of the Thule FTIR and the semi-autonomous measurement station is provided in Hannigan et al. (2009).

Measurements at both Eureka and Thule are made in the mid-infrared at a spectral resolution of 0.0035 cm^{-1} using a KBr beamsplitter that covers the spectral range of 700–5,000 cm^{-1}, a series of optical filters, and two photovoltaic detectors; a InSb detector (1,850–10,000 cm^{-1}), and a HgCdTe detector (600–6,000 cm^{-1}). Trace gas profiles and total column concentrations are retrieved from the measured spectra, and the data are regularly contributed to the Network for the Detection of Atmospheric Composition Change (NDACC; www.ndacc.org). In the following subsection, we describe the retrieval methods for estimating the trace-gas column concentrations from the measured solar-absorption spectra.

2.1.2. FTIR Retrieval Methods

The measured solar-absorption spectra from the Eureka and Thule FTIRs are processed using the SFIT4 retrieval algorithm (https://wiki.ucar.edu/display/sfit4/) that is an implementation of the Optimal Estimation Method described in Rodgers (2000) and it is based upon the older SFIT2 algorithm described in Pougatchev et al. (1995). The trace gas volume mixing ratio (VMR) profiles are iteratively adjusted until the difference between the calculated and measured solar-absorption spectra is minimized. The SFIT4 forward model is a line-by-line radiative transfer model that assumes a Voigt line shape profile and encompasses multiple atmospheric layers spanning the altitude of the instrument to 120 km above the surface.

For the retrievals of CO, C_2H_2, CH_3OH, and HCOOH spectroscopic parameters from the HITRAN 2008 line list database (Rothman et al., 2009) are used. For the retrieval of C_2H_6 pseudo-lines generated by G. C. Toon (Jet Propulsion Laboratory, California Institute of Technology, Pasadena, CA; available from https://mark4sun.jpl.nasa.gov/pseudo.html) are used for the spectral features of C_2H_6 and HITRAN 2008 is used for all other species following the approach of Franco et al. (2015). Similarly, in the retrieval of PAN pseudo-lines are used for the absorption features of PAN, while H_2O lines from the HITRAN 2016 line list database (Gordon et al., 2017) were used based on the recommendations in Mahieu et al. (2021), and HITRAN 2008 was used for all other interfering species. For the retrieval of H_2CO, the ATM16 line list was used (Toon et al., 2016). In these retrievals, pseudo-linelists were also used to supplement the spectroscopic databases in the case of any unresolved interfering features, namely those of carbon tetrachloride (CCl_4), chlorine nitrate ($ClONO_2$), CFC-12 (CCl_2F_2), HCFC-22 ($CHClF_2$), HFC-23 (CHF_3), and CFC-113 (CCl_2FCClF_2). Additionally, atmospheric temperature and pressure profiles are daily averages provided by the National Centers for Environmental Prediction, and the a priori profiles of each species are taken from a 40-year average (1980–2020) of the Whole Atmosphere Community Climate Model version 4 (Marsh et al., 2013).

The SFIT4 spectral microwindows, the interfering trace-gas species, and the corresponding references for each of the retrievals are provided in Table 1. CO and C_2H_6 are standard NDACC products, and are retrieved using specified NDACC Infrared Working Group (NDACC-IRWG; https://www2.acom.ucar.edu/irwg) recommendations and harmonized spectral microwindows (i.e., the same microwindows and retrieval approach are used for all sites in the network). The retrievals of CO and C_2H_6 are described in Lutsch et al. (2016) and Viatte et al. (2014) and references therein. C_2H_2, CH_3OH, HCOOH, H_2CO, and PAN are non-standard species, meaning that not all NDACC sites retrieve these products, however, these species are processed and retrieved in a similar manner as the standard products. The retrieval of C_2H_2 is described in Viatte et al. (2014, 2015), and the retrieval of H_2CO is described in Vigouroux et al. (2018, 2020), while detailed descriptions of the CH_3OH, HCOOH, and PAN retrievals are provided in Wizenberg, Strong, Jones, Lutsch, et al. (2023) and references therein.

Table 1
Spectral Microwindows and the Interfering Species Used for the Eureka and Thule Fourier Transform Infrared SFIT4 Retrievals and Corresponding References

Target species	Microwindows (cm^{-1})	Interfering species	References
CO	2,057.700–2,058.000, 2,069.560–2,069.760, 2,157.500–2,159.150	CO_2, H_2O, N_2O, O_3, OCS	Notholt et al. (2000), Y. Zhao et al. (2002), Viatte et al. (2014)
C_2H_2	3,250.430–3,250.770, 3,255.180–3,255.725, 3,304.825–3,305.350	H_2O, HDO	Paton-Walsh et al. (2010), Viatte et al. (2014)
C_2H_6	2,976.660–2,976.950, 2,983.200–2,983.550, 2,986.500–2,986.950	H_2O, O_3, CH_4	Notholt, Toon, Lehmann, et al. (1997), Viatte et al. (2014), Franco et al. (2015)
CH_3OH	992.000–998.700, 1,029.000–1,037.000	CO_2, H_2O, O_3, O_3(686), O_3(676), O_3(668), O_3(667)	Vigouroux et al. (2012), Viatte et al. (2014), Bader et al. (2014)
H_2CO	2,763.420–2,764.170, 2,765.650–2,766.010, 2,778.150–2,779.100, 2,780.650–2,782.000	HDO, CH_4, O_3, N_2O	Notholt, Toon, Lehmann, et al. (1997), Paton-Walsh et al. (2005), Viatte et al. (2014), Vigouroux et al. (2018)
HCOOH	1,102.000–1,109.000, 1,178.400–1,178.800	CCl_2F_2, CH_4, CHF_2Cl, H_2O, HDO, N_2O, NH_3, O_3	Zander et al. (2010), Vigouroux et al. (2012), Yamanouchi et al. (2020)
PAN	779.900–811.370	CO_2, CCl_4, CHF_2Cl, $ClONO_2$, CFC-113, H_2O, O_3	Mahieu et al. (2021)

For all retrievals, a full error analysis is performed for each site following Rodgers (2000). The total error budgets include contributions from forward model parameter errors, spectroscopic uncertainties, and measurement errors. The retrieval uncertainties are similar at both sites for all species. The random, systematic, and total uncertainties, as well as the degrees of freedom for signal (DOFS) for the Eureka and Thule FTIR retrievals are summarized in Table 2. The mean VMR averaging kernels for the Eureka and Thule retrievals are provided in Figures S1 and S2 in Supporting Information S1, and the total column averaging kernels and retrieval sensitivity for Eureka and Thule are provided in Figures S3 and S4 in Supporting Information S1, respectively. All of the trace gas retrievals display good vertical sensitivity throughout the troposphere, while CO and H_2CO display additional sensitivity to

Table 2
Mean Random, Systematic, and Total Retrieval Uncertainties and Degrees of Freedom for Signal (DOFS) of the Eureka and Thule Fourier Transform Infrared Retrievals

Species	Random uncertainty (%)	Systematic uncertainty (%)	Total uncertainty (%)	DOFS
CO	1	3	3.2	2–3
C_2H_2	5	1	5.1	1–1.5
C_2H_6	2.5	6	6.5	1.5–2
CH_3OH	4.5	12	12.8	1
H_2CO	10	13	16.4	1–1.5
HCOOH	3	9	9.5	1
PAN	20	10	22.4	1

the mid- and lower-stratosphere. All retrievals have a DOFS of 1 or greater, indicating that total column concentrations can be retrieved, while the retrieval of CO displays a higher DOFS of 2–3 on average, meaning that there is sufficient vertical information to derive partial columns from the retrievals.

2.2. GEOS-Chem Chemical Transport Model

The GCHP CTM (Eastham et al., 2018; Martin et al., 2022), version 14.1.1 was used in this study. GCHP is a new and highly parallelizable version of the GEOS-Chem model, allowing simulations to be completed in a much shorter duration when utilizing a high number of CPU cores. The model is run on the native NASA Goddard Earth Observing System cubed-sphere grid. The model simulation in this work was performed at a horizontal resolution of C48 (~2° × 2.5°), with 72 vertical layers from the surface to 0.01 hPa (approximately 80 km). The simulation is driven by assimilated meteorological fields from the Modern-Era Retrospective Analysis for Research and Applications, version 2 (MERRA-2; Gelaro et al., 2017) provided by the Global Modeling and Assimilation Office (GMAO) at the NASA Goddard Space Flight Center. The simulation covers the period of 1 January 2003 to 31 December 2021, with a 2-hourly output frequency. A model spin-up was performed for the full year of 2002 to provide the initial conditions for the simulation. Based on the recommendations provided in Philip et al. (2016), model transport and chemical operator time steps of 10 and 20 min, respectively, were selected to minimize simulation errors.

The emissions in the model are configured at run-time using the Harmonized Emissions Component (HEMCO; Lin et al., 2021), taking into account various inventories. All emissions fields are re-gridded by HEMCO from their native resolutions to the C48 cubed-sphere grid. Global anthropogenic emissions for the period of 1980–2019 are provided by CEDSv2, a comprehensive bottom-up inventory developed for use in Earth system models that utilizes regional and country-specific inventories to scale base emissions to produce trends over recent decades while maintaining a consistent methodology (Hoesly et al., 2018). These regional and country-scale inventories include the US EPA National Emissions Inventory for the United States, the European Monitoring and Evaluation Program Inventory for Europe, and the Emissions Database for Global Atmospheric Research for countries where national inventories are not available (Hoesly et al., 2018). For the years in the simulation which extend beyond the end of the CEDSv2 inventory (i.e., 2020 and 2021), the 2019 emissions are applied. In the case of C_2H_6, in the default configuration of the model anthropogenic emissions are sourced from the emissions inventory of Tzompa-Sosa et al. (2017) instead of CEDSv2, as other anthropogenic inventories were found to significantly underestimate C_2H_6 emissions. Additionally, biogenic emissions in the model are sourced from the Model of Emissions of Gasses and Aerosols from Nature (MEGAN; Guenther et al., 2012) version 2.1, and biomass burning emissions are provided by the Global Fire Assimilation System (GFAS; Kaiser et al., 2012) version 1.2. The GFASv1.2 inventory provides global fire emissions at a 3-hourly frequency on a 0.1° × 0.1° grid for the period of 2003–2021. The GFASv1.2 inventory was selected over the default Global Fire Emissions Database, version 4.1 inventory (GFEDv4.1; Van Der Werf et al., 2017) as it was found that northern mid- and high-latitude fires were better represented by GFAS when compared against satellite observations as discussed in Wizenberg, Strong, Jones, Lutsch, et al. (2023).

Emissions of C_2H_2 and HCOOH are absent from the current version of the GFAS inventory, so to approximate the emissions of these species we follow the approach described in Wizenberg, Strong, Jones, Lutsch, et al. (2023) and calculate the emission ratios relative to CO (in molar units) using values from Andreae (2019) for various biomass types (i.e., boreal forests, temperate forests, tropical forests, and grasslands). The GFEDv4.1 basis region map (available from: https://www.globalfiredata.org/data.html) was then used to allocate and apply the emissions globally in the model by scaling the existing GFAS CO fields by the pre-determined molar emission ratios in each region via the HEMCO module. An example of the resulting HCOOH emission flux and a map of the scaling ratios for August 2017 are provided as Figure S5 in Supporting Information S1. It should be noted that the GFEDv4.1 inventory was used during the model spin-up year of 2002, since the earliest year available for the GFASv1.2 inventory is 2003.

2.3. Trend Analysis

The Eureka and Thule ground-based time-series span 14 years (2006–2020) and 23 years (1999–2022), respectively, allowing long-term trends to be assessed. Since the time-series of each trace-gas species contains both intra-annual variability (seasonal cycles) and inter-annual variability (long-term trends), we apply Fourier

series fitting of multiple orders to the total column time-series data from the two Arctic FTIRs, and the simulated columns from GCHP following the method of Friedrich et al. (2020), taking into account the auto-correlation in the time-series data. We apply a least-squares fit to the data with a function F of the form (Gardiner et al., 2008):

$$F(t, a, \boldsymbol{b}) = at + V(t, \boldsymbol{b}) \quad (1)$$

where a is the annual trend in the data, t is the time measured in years, and $V(t, \boldsymbol{b})$ is the Fourier series component that is given by:

$$V(t, \boldsymbol{b}) = b_0 + b_1 \cos 2\pi t + b_2 \sin 2\pi t + b_3 \cos 4\pi t + b_4 \sin 4\pi t + \ldots \quad (2)$$

where b_0 to b_n are the Fourier series parameters contained in the vector $\boldsymbol{b}$. Fourier series models of this type allow for the underlying periodicity of the data to be captured while also reducing the impact of sparse data. This method also allows for regular gaps in the data, such as during the polar night, to be accounted for without causing a discontinuity in the intra-annual fit function (Gardiner et al., 2008). In this study, a Fourier series of order 3 was used for all fits, with the exception of CH_3OH and H_2CO where a Fourier series of order 2 was used because an appropriate fit to the FTIR data could not be established with order 3 due to either the sparseness of the data set or larger short-term variability in the measured total columns. To derive the confidence intervals (CIs) for the fitted trends, we apply bootstrap resampling with Q = 5,000 (the number of bootstrapping ensemble members). Bootstrap resampling allows for a statistically robust treatment of non-normally distributed data sets, and this approach has been widely used to evaluate the CIs of trends derived from FTIR measurements (Franco et al., 2016a; Friedrich et al., 2020; Gardiner et al., 2008; Gatz & Smith, 1995; Yamanouchi et al., 2021).

Since the FTIR and GCHP total column time-series contain transient events such as biomass burning enhancements, we identify these events using Fourier fit following Lutsch et al. (2020) and Zellweger et al. (2009). The fitted Fourier series function is first subtracted from the data to obtain the residuals, and then assuming a normal distribution of the residuals about zero, the negative residuals are mirrored into positive values (by taking the absolute value). A cutoff threshold of 2σ is then applied to the data based on the standard deviation of the absolute residuals, and another Fourier series fit is performed with the identified enhancements removed. The trend analysis was performed twice; first on the full data set, and then on time-series with the enhancements removed. The trends derived from the "enhancement-removed" Fourier fit are likely more representative of the true long-term variability in the background concentrations of each trace-gas species, however, comparing the differences between the Fourier fits (i.e., with and without enhancements) may highlight how significantly each time-series is impacted by wildfires and other transient events.

3. Results and Discussion

3.1. FTIR-Derived Seasonal Cycles

In this section, we evaluate the seasonal cycles of CO, C_2H_2, C_2H_6, CH_3OH, HCOOH, H_2CO, and PAN derived from the ground-based FTIR measurements at Eureka and Thule. The retrieved total column time-series of these seven tropospheric species and the corresponding monthly means calculated across all years are shown for Eureka and Thule in Figures 1 and 2, respectively.

3.1.1. CO

The seasonal cycle of CO is shown for Eureka in Figure 1a, and for Thule in Figure 2a. CO displays a strong seasonal cycle that is consistent at both Arctic sites, with the largest mean CO columns observed during the late winter and early spring (February to April), and a minimum during the summer in July. The mean maximum total columns are approximately 2.0×10^{18} molec. cm^{-2} and 2.1×10^{18} molec. cm^{-2}, while the mean minimum total columns are around 1.5×10^{18} molec. cm^{-2} and 1.6×10^{18} molec. cm^{-2} at Eureka and Thule, respectively. The primary sources of CO are fossil fuel combustion and the oxidation of VOCs and CH_4, which is transported to the Arctic from mid-latitude sources, with biomass burning being a significant periodic source during the late summer months (Holloway et al., 2000; Lutsch et al., 2020; Yurganov et al., 1995). CO is primarily removed from the atmosphere through oxidation by the hydroxyl radical (OH), which consumes OH and yields CO_2, making CO an indirect greenhouse gas. During polar night, no OH is present in the Arctic troposphere and the atmospheric

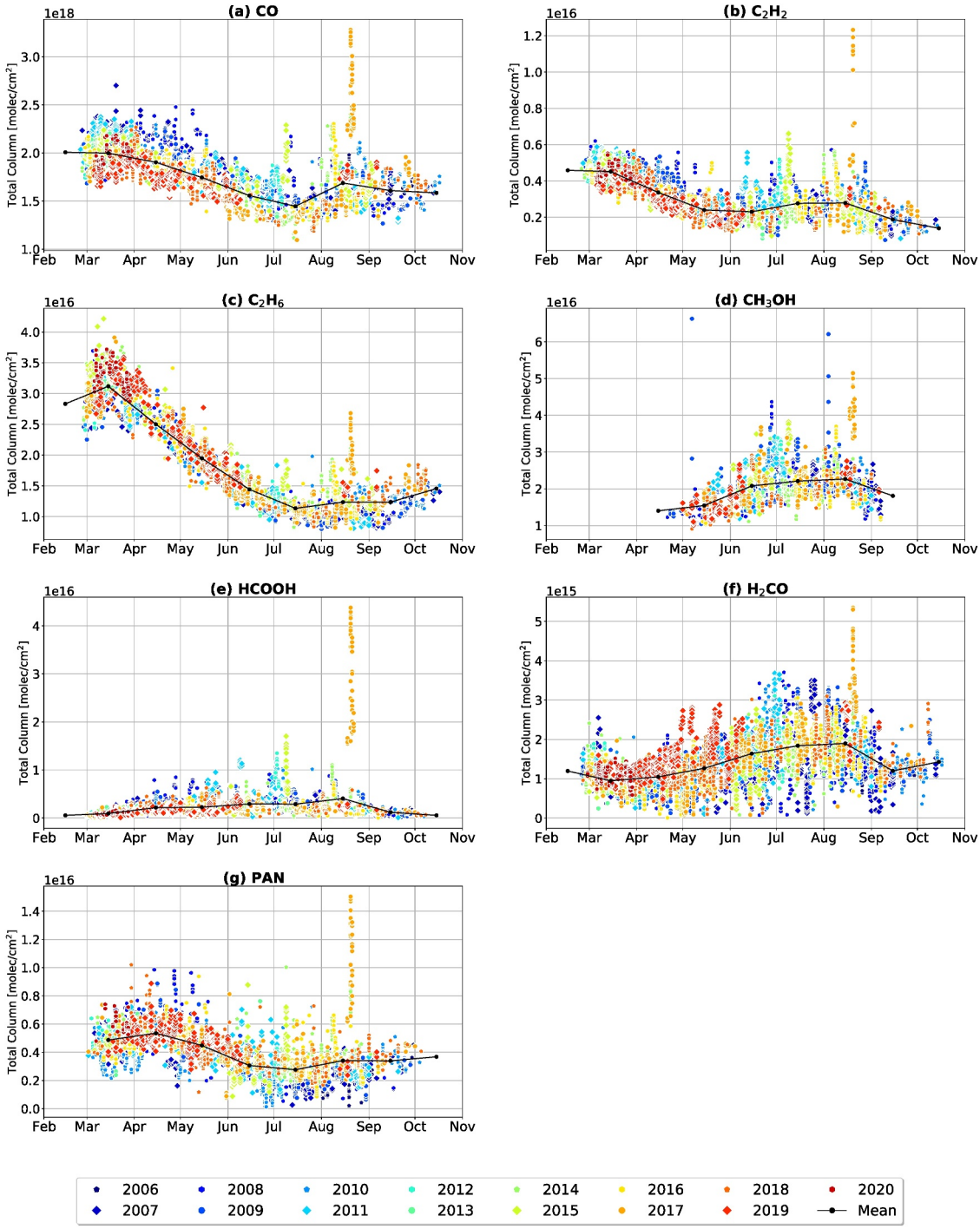

Figure 1. Total column time series of (a) CO, (b) C_2H_2, (c) C_2H_6, (d) CH_3OH, (e) HCOOH, (f) H_2CO, and (g) PAN retrieved from Bruker 125HR measurements at Eureka for the period of 2006–2020. Measurements from each year are plotted in differing colors and marker styles to better highlight enhancements and anomalies. The monthly means across all years are denoted by the black line.

lifetime of CO can be on the order of several months (Holloway et al., 2000). As a consequence, transported mid-latitude CO tends to accumulate in high concentrations, resulting in the peak in the observed total columns in the late winter and early spring months (Holloway et al., 2000; Notholt, Toon, Stordal, et al., 1997; Stohl, 2006). As polar night ends and sunlight gradually returns to the high Arctic, the observed CO total columns rapidly decrease,

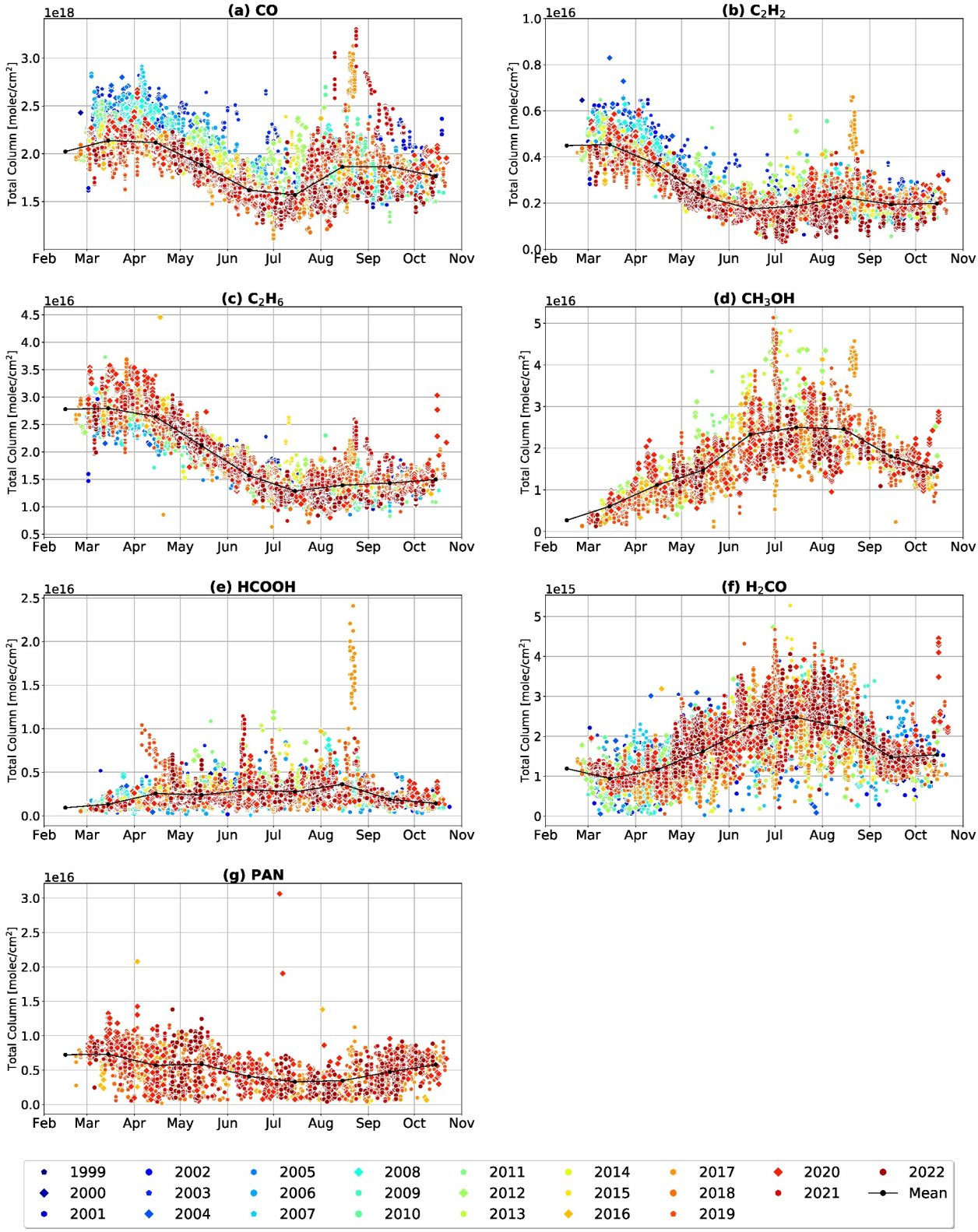

Figure 2. Total column time series of (a) CO, (b) C_2H_2, (c) C_2H_6, (d) CH_3OH, (e) HCOOH, (f) H_2CO, and (g) PAN retrieved from the Bruker 120M (1999–2015) and Bruker 125HR (2015–2022) measurements at Thule. Measurements from each year are plotted in differing colors and marker styles to better highlight enhancements and anomalies. The monthly means across all years are denoted by the black line.

leading to a minimum in July. Periodic enhancements in the CO total columns can be seen in August at both Eureka and Thule, resulting from the influence of transported biomass burning plumes.

3.1.2. C_2H_2

The total column time-series and monthly means for C_2H_2 are shown for Eureka and Thule in Figures 1b and 2b, respectively. C_2H_2 presents a very similar seasonal cycle to CO at both Eureka and Thule, with a maxima in the observed total columns in February and March, and a minima in the total columns during June. The mean maximum columns are approximately 4.5×10^{15} molec. cm^{-2} at both sites, while the mean minimum total columns are 2.5×10^{15} molec. cm^{-2} and 1.8×10^{15} molec. cm^{-2} at Eureka and Thule, respectively. C_2H_2 is primarily emitted from biofuel and fossil fuel combustion, and is co-emitted with CO in many cases. Biomass burning is also a notable source of C_2H_2 to the high Arctic, which is clearly seen at both sites during August in Figures 1b and 2b (Viatte et al., 2014, 2015). Like CO, the primary atmospheric sink of C_2H_2 is oxidation by OH, which is a crucial driver of its strong seasonality at high latitudes. As a result, C_2H_2 is strongly correlated with CO in the atmosphere as they share very similar sources and sinks which is evidenced in the seasonal cycles at both Arctic sites (Duflot et al., 2015; Notholt, Toon, Stordal, et al., 1997; Xiao et al., 2007).

3.1.3. C_2H_6

The seasonal cycle and monthly means of C_2H_6 are plotted for Eureka and Thule in Figures 1c and 2c, respectively. C_2H_6 displays a strong seasonal cycle at both sites akin to that of CO and C_2H_2, with the largest observed total columns in February and March, and the smallest columns in July. The observed seasonal cycle is broadly consistent with that reported at Ny-Ålesund, Svalbard by Notholt, Toon, Stordal, et al. (1997). The mean maximum columns are 3.1×10^{16} molec. cm^{-2} and 2.8×10^{16} molec. cm^{-2}, while the mean minimum total columns are 1.1×10^{16} molec. cm^{-2} and 1.3×10^{16} molec. cm^{-2} at Eureka and Thule, respectively. C_2H_6 is the most abundant non-methane hydrocarbon in the atmosphere, and is an important precursor to tropospheric ozone and PAN through its oxidation in the presence of nitrogen oxide radicals ($NO_x = NO + NO_2$) in polluted airmasses (Fischer et al., 2014; Franco et al., 2016a). C_2H_6 also acts as an indirect greenhouse gas through its influence on the global lifetime of methane (CH_4) as a result of its removal from the atmosphere by OH. In contrast to CO and C_2H_2, C_2H_6 differs in that it is primarily emitted from the various stages of natural gas production and distribution as opposed to the direct combustion of fossil fuels (Franco et al., 2016a; Friedrich et al., 2020; Xiao et al., 2008). The main sources of C_2H_6 to the high Arctic are biomass burning and transported mid-latitude pollution, and it is primarily removed from the Arctic troposphere through oxidation by OH which strongly modulates the observed seasonal cycles at Eureka and Thule.

3.1.4. CH_3OH

The total column time-series and the corresponding monthly means of CH_3OH calculated across all years are shown in Figures 1d and 2d for Eureka and Thule, respectively. CH_3OH displays a clear seasonal cycle at Eureka and Thule, with the smallest total columns in the spring and fall months, and the largest observed columns in the summertime between June and August. The mean maximum columns are 2.3×10^{16} molec. cm^{-2} and 2.5×10^{16} molec. cm^{-2}, and the mean minimum columns are 1.4×10^{16} and 2.7×10^{15} molec. cm^{-2} at Eureka and Thule, respectively. It should be noted that CH_3OH measurements at Thule extend earlier into the year than at Eureka, with measurements available beginning in February at Thule and April at Eureka. Retrievals during the early year often fail to converge at Eureka due to the low abundance of CH_3OH and strong interference from O_3 in the early spring. The mean columns in April at Thule are approximately 1.1×10^{16} molec. cm^{-2}, which is broadly consistent with the mean minimum columns at Eureka. CH_3OH is the second-most abundant organic gas (after CH_4) found in the global remote atmosphere (Stavrakou et al., 2011). It is primarily emitted biogenically from plants during their growth stage (and to a lesser extent when they decay), however, it is also emitted from biomass burning (Fall & Benson, 1996; Holzinger et al., 1999; MacDonald & Fall, 1993; Wells et al., 2014). The oceans can also serve as a source of CH_3OH, however, globally they are thought to represent a small net sink (Bates et al., 2021). Through its oxidation, CH_3OH influences global OH concentrations, producing the hydroperoxyl radical (HO_2) and H_2CO, and it can influence the budget of tropospheric O_3 (Folberth et al., 2006; Tie et al., 2003). As a result, the seasonal cycle at both Eureka and Thule is largely correlated with the growth cycle of plants and vegetation, leading to the highest observed columns during the summer months, and lower columns during the early spring and fall. Biomass burning enhancements are visible in the time-series at Eureka and Thule

in Figures 1d and 2d, however, these enhancements tend to be more moderate than for some of the other biomass burning tracer species such as CO, and C_2H_2.

3.1.5. HCOOH

The seasonal cycle and monthly means of HCOOH are shown in Figures 1e and 2e for Eureka and Thule, respectively. HCOOH displays a similar seasonal cycle as CH_3OH albeit less pronounced at the two Arctic sites, with smaller total columns seen in the spring and fall, and larger columns on average during the summer. The mean maximum columns across all years at Eureka and Thule are 4.1×10^{15} molec. cm^{-2} and 3.6×10^{15} molec. cm^{-2}, and the mean minimum columns are 5.6×10^{14} and 9.3×10^{14} molec. cm^{-2}, respectively. HCOOH is the most abundant carboxylic acid in the global troposphere, with a relatively short lifetime typically on the order of 4 days (Stavrakou et al., 2012). Sources of HCOOH include anthropogenic emissions, direct emissions from plant leaves, and biomass burning, while the main sinks of HCOOH are oxidation by OH, as well as dry and wet deposition (Chameides & Davis, 1983; Chen et al., 2021). As a result of its removal from the atmosphere by dry and wet deposition, HCOOH directly contributes to soil and rainwater acidity in remote regions such as the Arctic (Paulot et al., 2011; Stavrakou et al., 2012). As with CH_3OH, emissions from plants are an important driver of the seasonal cycle at Eureka and Thule. Additionally, a study of ground-level HCOOH concentrations at Alert, Nunavut by Mungall et al. (2018) suggests that there may be a complex system of local photochemical sources of HCOOH in the Arctic, however these are currently not well quantified, and the magnitude of their influence on the overall budget is unclear. Very large enhancements in the total columns resulting from transported biomass burning plumes can also be seen in the late summer months at both Eureka and Thule in Figures 1e and 2e, respectively.

3.1.6. H_2CO

The total columns and monthly means of H_2CO are shown in Figures 1f and 2f for Eureka and Thule, respectively. H_2CO displays a distinct seasonal cycle at both FTIR sites, with lower total columns in the spring and fall, and higher total columns on average during the summer months. The mean maximum columns across all years at Eureka and Thule are 1.9×10^{15} molec. cm^{-2} and 2.5×10^{15} molec. cm^{-2}, respectively, and mean minimum columns of approximately 9.5×10^{14} molec. cm^{-2} observed at both sites. H_2CO is one of the most abundant VOCs in the atmosphere, and it plays an important role in atmospheric photochemistry and air quality (Luecken et al., 2012). H_2CO is directly emitted from a variety of anthropogenic and natural sources including fossil fuel combustion, biomass burning, and biogenic emissions from plants and soil, but it is also produced in large quantities via secondary formation in the atmosphere through the oxidation of CH_4 and non-methane volatile organic compounds (NMVOCs) (Holzinger et al., 1999; Luecken et al., 2012, 2018; Wittrock et al., 2006). It is primarily removed via its reaction with OH yielding HO_2 radicals, which can subsequently be converted back into OH, meaning that OH plays an important role in both the formation and removal of H_2CO from the atmosphere (Mahajan et al., 2010; Nussbaumer et al., 2021; Wittrock et al., 2006). As a result, the seasonal cycle of H_2CO at Eureka and Thule is largely driven by the availability of sunlight and OH in the Arctic atmosphere. Biogenic emissions of H_2CO from high-latitude boreal forests also contribute to the observed seasonal maxima in the summertime (T. Zhao et al., 2022). The seasonal cycles in the H_2CO total columns at Eureka and Thule resemble that which was reported by Notholt, Toon, Stordal, et al. (1997). Some biomass burning enhancements are visible in the time-series at Eureka and Thule between June to August. However, the influence of wildfires on the overall H_2CO columns during the summertime appears to be relatively small, particularly at Thule.

3.1.7. PAN

The seasonal cycle and monthly means of PAN are shown for Eureka and Thule in Figures 1g and 2g, respectively. PAN exhibits a seasonal cycle similar in appearance to CO and C_2H_2, with the largest columns observed between February and March which corresponds with the peak in the Arctic Haze pollution phenomena (Law & Stohl, 2007), and the smallest total columns during June to July. The mean maximum columns across all years are 5.4×10^{15} molec. cm^{-2} and 7.3×10^{15} molec. cm^{-2}, and the mean minimum columns are 2.8×10^{15} and 3.3×10^{15} molec. cm^{-2} at Eureka and Thule, respectively. PAN's atmospheric lifetime is highly variable, ranging from approximately 1 hr at 298 K to several months at the colder temperatures found in the upper troposphere and lower stratosphere (Bridier et al., 1991; Jacob, 2000; Moxim et al., 1996; Orlando et al., 1992; Talukdar et al., 1995). PAN is not directly emitted, but rather it results from secondary formation through the oxidation of

Table 3
Fitted Trends Derived From Daily-Mean Fourier Transform Infrared Total Columns at Eureka and Thule in Relative Units (% year^{-1})

	Eureka, Nunavut (2006–2020)		Thule, Greenland (1999–2022)	
Species	Trend (% year^{-1})	Trend w/o enhancements (% year^{-1})	Trend (% year^{-1})	Trend w/o enhancements (% year^{-1})
CO	**−0.84** (−1.07, −0.62)	**−1.10** (−1.23, −0.97)	**−0.76** (−0.93, −0.58)	**−0.89** (−0.99, −0.79)
C_2H_2	**−2.20**[a] (−3.03, −1.34)	**−2.57**[a] (−3.14, −1.96)	**−1.71** (−2.03, −1.38)	**−1.61** (−1.83, −1.39)
C_2H_6	**1.07** (0.76, 1.38)	**0.98** (0.77, 1.18)	**0.61** (0.39, 0.84)	**0.56** (0.42, 0.70)
CH_3OH	−0.24[b] (−1.01, 0.51)	**−0.57**[b] (−1.07, −0.08)	**−2.02**[c] (−2.73, −1.30)	**−1.64**[c] (−2.09, −1.20)
HCOOH	−2.14 (−5.09, 0.82)	**−2.98** (−4.13, −1.82)	0.26 (−0.58, 1.08)	−0.17 (−0.68, 0.35)
H_2CO	**2.02** (1.20, 2.84)	**1.91** (1.42, 2.40)	**1.19** (0.66, 1.72)	**0.97** (0.65, 1.29)
PAN	**2.17** (1.28, 3.05)	**2.13** (1.64, 2.62)	2.20[d] (−0.31, 4.61)	1.29[d] (−0.59, 3.22)

Note. The 95% confidence intervals calculated from bootstrap resampling with $Q = 5{,}000$ ensemble members are provided below each value in parentheses. Trends that are considered statistically significant (i.e., the 95% confidence intervals do not overlap with zero) are in bold. [a]The time-series of C_2H_2 at Eureka begins in July 2007. [b]Only 1 day of CH_3OH total columns was available at Eureka in 2020, so these data are excluded from the analysis. [c]The time-series of CH_3OH at Thule begins in March 2011. [d]The time-series of PAN at Thule begins in May 2015.

NMVOCs such as acetone (C_3H_6O), acetaldehyde (CH_3CHO), and methylglyoxal ($C_3H_4O_2$) in the presence of NO_x. These PAN precursors have both anthropogenic and natural sources including direct emissions from human activities and industry, and biomass burning (Akagi et al., 2011; Coheur et al., 2009; Fischer et al., 2014; Jacob, 2000; Juncosa Calahorrano et al., 2020; Liu et al., 2016). As a result, PAN is primarily formed in polluted mid-latitude regions, particularly during the springtime, and then it undergoes long-range transport to the high-Arctic region (Fischer et al., 2014; Moxim et al., 1996). Consequently, this leads to an accumulation of high concentrations of PAN during polar night and the early spring (visible in Figures 1g and 2g). The temperature dependence of PAN's atmospheric lifetime is a major driver of the observed seasonal cycle at the two Arctic sites, leading to a steady decrease in the observed PAN columns at both sites beginning in April and reaching a minimum in July. Biomass burning enhancements can be seen to some extent at both Eureka and Thule, however, the influence of wildfires on the PAN total columns in the late summer months appears to be more significant at Eureka.

3.2. FTIR-Derived Trends

The Fourier series fitting approach described in Section 2.3 was applied to the daily-mean total columns of all species at each site. The fitted trends and 95% CIs in % year^{-1} are summarized in Table 3, and are plotted in Figures 3 and 4 for Eureka and Thule, respectively. In the text, we provide the trend values and 95% CIs in relative units. A version of Table 3 in absolute units (i.e., molec. cm^{-2} year^{-1}) is included in Supporting Information S1 as Table S1, and the reader can refer to this table for the absolute values of the trends.

3.2.1. CO

CO at Eureka was found to have a clear negative trend of −0.84 [−1.07, −0.62]% year^{-1} (slope [lower 95% CI, upper 95% CI]) over the period of 2006–2020 (see Figure 3a). Similarly, at Thule a negative trend of −0.76 [−0.94, −0.58]% year^{-1} is found for the period of 1999–2022 (see Figure 4a). If enhancement events are excluded from the time-series, we obtain slightly more negative trends of −1.10 [−1.23, −0.97]% year^{-1} and −0.89% [−0.99, −0.79]% year^{-1} at Eureka and Thule, respectively. The decrease in the fitted trends when removing enhancement events suggests that larger and more frequent enhancement events are occurring in the latter portion of the data record at Eureka and Thule, and this can be seen to some extent in Figures 3a and 4a.

The observed trends at Eureka and Thule are consistent with recent satellite-derived CO trends over the last two decades, which are generally in the range of −0.5% year^{-1} to −1% year^{-1} in the northern hemisphere depending on the period of study (Buchholz et al., 2021; Worden et al., 2013; X. Zhang et al., 2020). A recent trend study using ground-based FTIR data at Toronto by Yamanouchi et al. (2021) found a CO trend of −0.90 ± 0.07% year^{-1} over the period of 2002–2019, and an older study by Angelbratt et al. (2011) derived CO trends of −0.45 ± 0.16% year^{-1}, −1.00 ± 0.24% year^{-1}, −0.62 ± 0.19% year^{-1}, and −0.61 ± 0.16% year^{-1} from NDACC FTIR measurements in Europe at Jungfraujoch, Zugspitze, Harestua and Kiruna over the period of 1996–2006,

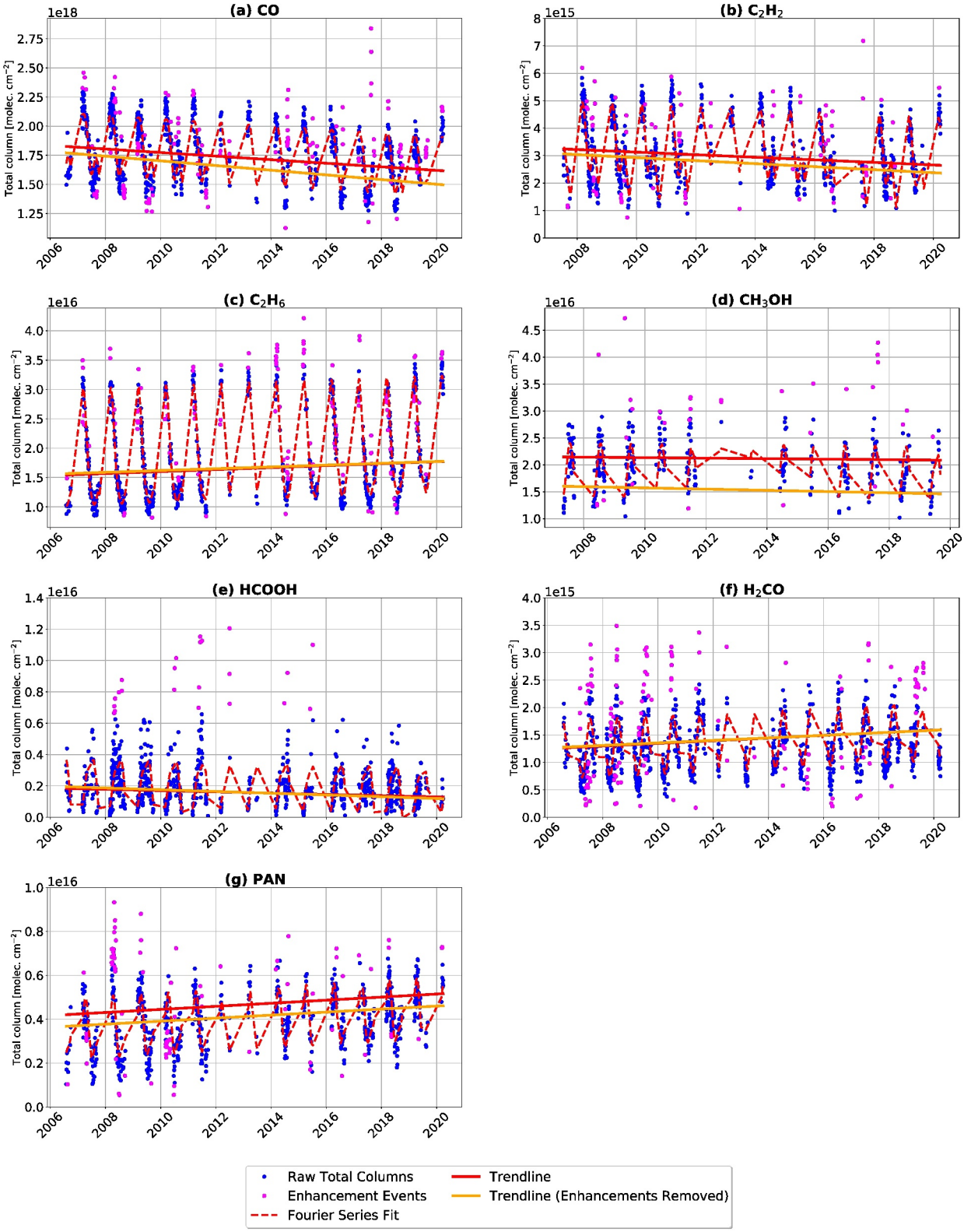

Figure 3. Fourier series fit and the corresponding trendlines plotted over the total column time-series of (a) CO, (b) C_2H_2, (c) C_2H_6, (d) CH_3OH, (e) HCOOH, (f) H_2CO, and (g) PAN retrieved from Bruker 125HR measurements at Eureka. Note that the *y*-axis limits of some panels have been adjusted relative to Figure 1 for increased visibility of the fitted trends.

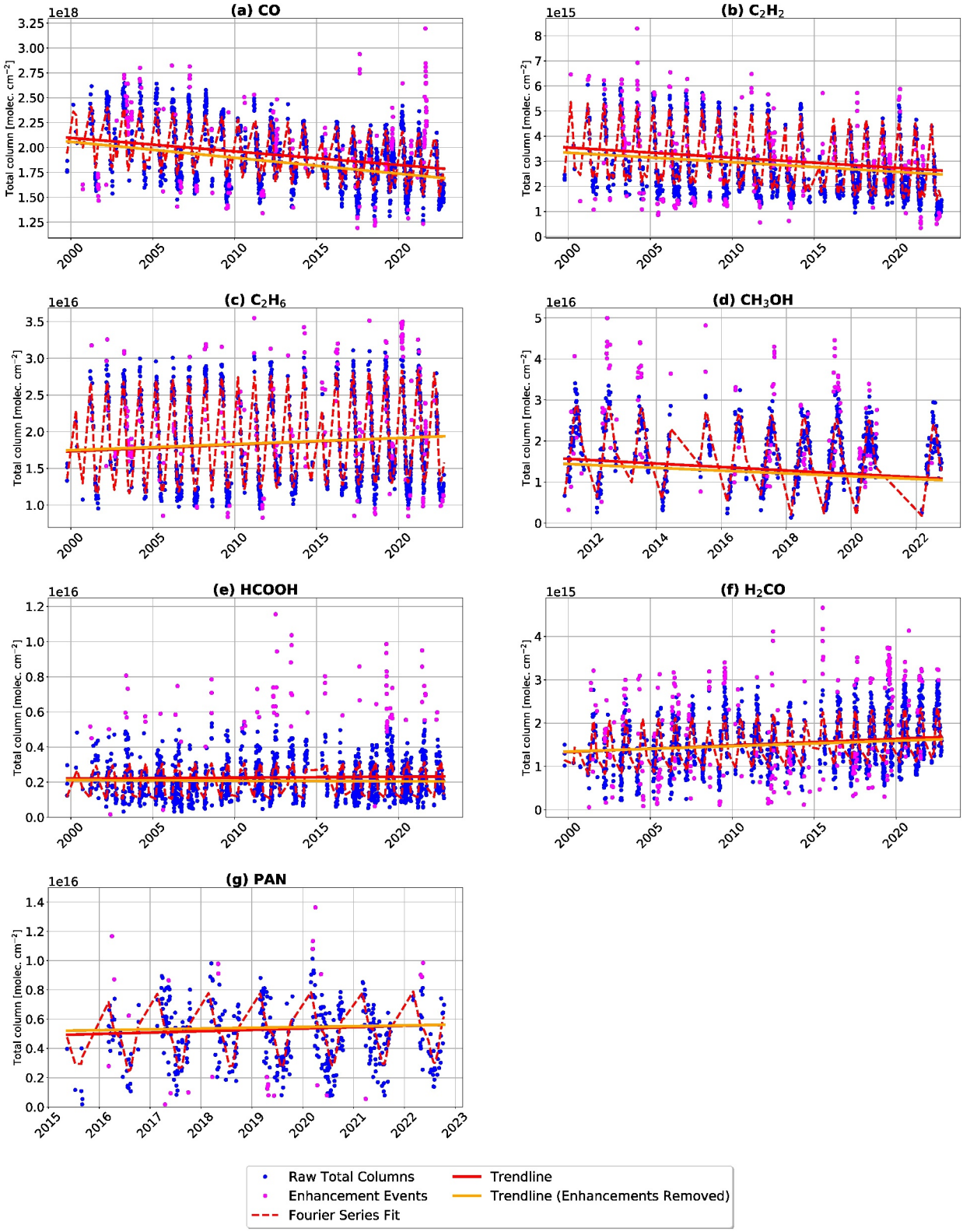

Figure 4. Fourier series fit and the corresponding trendlines plotted over the total column time-series of (a) CO, (b) C_2H_2, (c) C_2H_6, (d) CH_3OH, (e) HCOOH, (f) H_2CO, and (g) PAN retrieved from the Bruker 120M (1999–2015) and Bruker 125HR (2015–2022) measurements at Thule. Note that the *y*-axis limits of some panels have been adjusted relative to Figure 2 for increased visibility of the fitted trends.

respectively. The observed downward trend in CO is believed to be largely driven by reductions in fossil fuel-based emissions resulting from the increased efficiency of internal combustion engines in recent years (Buchholz et al., 2021; Worden et al., 2013; Yamanouchi et al., 2021).

3.2.2. C_2H_2

A negative trend of −2.20 [−3.03, −1.34]% year^{-1} over the period of 2007–2020 was found for C_2H_2 at Eureka (Figure 3b). At Thule, a negative C_2H_2 trend of −1.71 [−2.03, −1.38]% year^{-1} is seen during the period of 1999–2022 (Figure 4b). Excluding enhancement events, we obtain a stronger negative trend at Eureka of −2.57 [−3.14, −1.96]% year^{-1} but the trend at Thule becomes slightly less negative with a value of −1.61 [−1.83, −1.39]% year^{-1}. At Eureka, the largest enhancement events occur in the latter half of the 2007–2020 time-series, while at Thule a very large C_2H_2 enhancement event occurred in 2004 (shown in Figure 4b), leading to the slight difference in the trends with and without enhancements at the two sites.

Since CO and C_2H_2 are co-emitted from fossil fuel combustion and are highly correlated in the atmosphere (Xiao et al., 2007), the observed negative trends at Eureka and Thule are anticipated, and are broadly consistent with recent studies. Yamanouchi et al. (2021) reported a C_2H_2 trend of −1.12 ± 0.30% year^{-1} derived from FTIR measurements at Toronto in the period of 2002–2019. Similarly, Bernath et al. (2020) report a trend of −1.70 ± 0.38% year^{-1} derived from ACE-FTS measurements between 30°N and 90°N in the period of 2004–2020.

3.2.3. C_2H_6

An positive trend in C_2H_6 is observed at both high Arctic sites. At Eureka, a trend of 1.07 [0.76, 1.38]% year^{-1} in the period of 2006–2020 was found (Figure 3c). At Thule, a trend of 0.61 [0.39, 0.84]% year^{-1} is observed between 1999 and 2022 (Figure 4c). If a fit is performed on the Thule time-series over the same period as the Eureka data set (August 2006 to March 2020), a more strongly positive trend of 1.66 [1.26, 2.06]% year^{-1} is found. When excluding enhancement events, the positive trends at both sites decrease slightly to 0.98 [0.77, 1.18]% year^{-1} and 0.56 [0.42, 0.70]% year^{-1} at Eureka and Thule, respectively. An apparent brief decline in C_2H_6 can be seen in the Eureka time-series between 2015 and 2018 before returning to higher levels in 2019, however this feature is not discernible in the Thule time-series and the cause is unclear.

Positive trends in atmospheric C_2H_6 concentrations in the Northern Hemisphere after 2009 have been widely reported in recent studies (e.g., Bernath et al., 2020; Franco et al., 2016a; Friedrich et al., 2020; Maddanu & Proietti, 2023; Yamanouchi et al., 2021), and this has been linked to significant increases in oil and natural gas production and distribution in the United States (Franco et al., 2015, 2016a; Helmig et al., 2016; Monks et al., 2018; Tzompa-Sosa et al., 2017). Franco et al. (2016a) obtained positive trends of approximately 3% year^{-1} at Eureka and Thule between 2009 and 2014, and if the methodology presented here is used for the same time period, we obtain consistent trends of 3.63 [2.53, 4.74]% year^{-1} and 2.93 [1.72, 4.08]% year^{-1} at Eureka and Thule, respectively. Yamanouchi et al. (2021) report a positive trend of 1.19 ± 0.27% year^{-1} determined from FTIR measurements at Toronto between 2009 and 2019, which is broadly consistent with the trends presented here for Eureka and Thule. Lastly, Bernath et al. (2020) found a positive C_2H_6 trend of 1.26 ± 0.30% year^{-1} in the northern hemisphere between 30°N and 90°N using ACE-FTS data in the period of 2004–2020, which falls within the range of uncertainty of the fitted trend at Eureka.

3.2.4. CH_3OH

The measured CH_3OH total columns at Eureka show no statistically significant trend in the period of 2006–2019, with a fitted slope of −0.24 [−1.01, 0.51]% year^{-1} (see Figure 3d). At Thule, a significant negative trend of −2.02 [−2.73, −1.30]% year^{-1} was obtained for 2011–2022 (shown in Figure 4d). If the Eureka time-series is truncated to 2011–2020, a more strongly negative slope of −1.04 [−2.71, 0.49]% year^{-1} is obtained, however the trend is still not considered statistically significant. When enhancement events are excluded from the Fourier series fit, a statistically significant negative trend is found at Eureka of −0.57 [−1.07, −0.08]% year^{-1} between 2006 and 2020. At Thule, the trend becomes slightly less negative when enhancements are removed, with a slope of −1.64 [−2.09, −1.20]% year^{-1}.

It is currently uncertain what factors might drive a negative trend in CH_3OH in the Arctic region, as the general understanding of the local sources and sinks at these high latitudes is relatively limited. Bernath et al. (2020) found no trend in CH_3OH in ACE-FTS measurements between 2004 and 2020, however, their trend analysis was limited to the region of −60°S to 60°N. Their results also indicate high concentrations of CH_3OH between 80°N and 90°N, but this was not included in their discussion. Similarly, Yamanouchi et al. (2021) found no statistically significant trend in CH_3OH at Toronto over the period of 2002–2019. In remote regions such as the Arctic, the ocean serves as a net sink of atmospheric CH_3OH due to deposition on the sea surface and subsequent uptake by marine bacteria (Bates et al., 2021; M. Yang et al., 2013). A recent study by Wohl et al. (2022) that measured dissolved concentrations of CH_3OH and other VOCs in regions of varying ice coverage in the Canadian Arctic ocean suggests a complex interplay between sea ice coverage and the strength of the ocean as a sink for CH_3OH. It is believed that as sea ice coverage decreases and the air-to-sea flux in the Arctic increases, the ocean will become a stronger sink of oxygenated VOCs, causing a reduction in their atmospheric concentrations (Wohl et al., 2022). It is possible that this may be a driver of the observed CH_3OH trends at Eureka and Thule, however further study is needed.

3.2.5. HCOOH

No statistically significant trend is found in the measured HCOOH total columns at Eureka when all data are included, with a fitted slope of −2.14 [−5.09, 0.82]% $year^{-1}$ (see Figure 3e). When enhancement events are excluded from the Fourier series fit at Eureka, a significant negative trend of −2.98 [−4.13, −1.82]% $year^{-1}$ is found between 2006 and 2020. At Thule, no statistically significant trends are found with or without enhancement events, with slopes of 0.26 [−0.58, 1.08]% $year^{-1}$ and −0.17 [−0.68, 0.35]% $year^{-1}$, respectively (shown in Figure 4e).

To our knowledge, no studies have reported long-term HCOOH trends in the high Arctic. Yamanouchi et al. (2021) found negative HCOOH trends of −2.15 ± 0.64% $year^{-1}$ with enhancements and −0.73 ± 0.53% $year^{-1}$ without enhancements at Toronto in the period of 2002–2019, which are more negative than the trend derived from ACE-FTS measurements of −0.51 ± 0.28% $year^{-1}$ in the range of 60°S to 60°N between 2004 and 2020 reported by Bernath et al. (2020). These reported negative trends broadly agree with the observations at Eureka, but they may not be fully representative of trends in the Arctic. Several studies in the Arctic have found that snowpack photochemistry is an important local source of HCOOH in the region, and that the high measured concentrations could not be sustained by transport alone (Dibb & Arsenault, 2002; Mungall et al., 2018; Paulot et al., 2011). Mungall et al. (2018) found that surface HCOOH concentrations measured during early summer 2016 at Alert, Nunavut displayed occasional excursions to extremely high values and a strong diurnal cycle during sunny conditions, indicating a notable photochemical source near the ground and highlighting the complex nature of local HCOOH sources. The extent to which these local sources may influence the measured atmospheric concentrations and trends at Eureka and Thule is currently not well quantified.

3.2.6. H_2CO

Positive trends were found for H_2CO at Eureka and Thule. At Eureka, a trend of 2.02 [1.20, 2.84]% $year^{-1}$ was found for the period of 2006–2020 (see Figure 3f). At Thule, a trend of 1.19 [0.66, 1.72]% $year^{-1}$ was found between 1999 and 2022 (Figure 4f). If enhancement events are excluded, the slope of the trends decrease slightly to 1.91 [1.42, 2.40]% $year^{-1}$ and 0.97 [0.65, 1.29]% $year^{-1}$ at Eureka and Thule, respectively.

Both positive and negative H_2CO trends have been reported in the literature, and the direction of the trends appears to vary based on region. Vigouroux et al. (2018) found no statistically significant trends at Eureka or Thule, but obtained negative trends at mid-latitude FTIR sites, with trends of −0.39 ± 0.33% $year^{-1}$ and −0.96 ± 0.51% $year^{-1}$ at St. Petersburg and Mexico City, respectively, and strong positive trends of 1.73 ± 1.52% $year^{-1}$ and 1.58 ± 0.52% $year^{-1}$ the tropical sites of Izana (2005–2016) and Saint-Denis (2004–2013), respectively. Yamanouchi et al. (2021) found a slightly negative trend at Toronto of −0.43 ± 0.25% $year^{-1}$ only after removing enhancement events. Franco et al. (2016b) found a positive trend at Jungfraujoch of 0.81 ± 0.62% $year^{-1}$ using FTIR data between 2003 and 2015, which they suggest is likely related to increases in atmospheric CH_4 concentrations. Bernath et al. (2020) found a positive but non-significant trend in stratospheric H_2CO of 0.18 ± 0.18% $year^{-1}$ between 30°S and 30°N with ACE-FTS, but a positive significant trend in the troposphere in the same region. Lastly, De Smedt et al. (2015) found strongly positive trends over Asia driven by

greater emissions, but negative trends over Europe and North America using measurements from the Ozone Monitoring Instrument (OMI) and the Global Ozone Monitoring Experiment-2 (GOME-2) between 2004 and 2014. The observed positive trends at Eureka and Thule may be driven in-part by greater emissions from Asia coupled with steadily rising CH_4 concentrations, however a broader study of these observed trends at high northern latitudes may be needed.

3.2.7. PAN

A clear upwards trend of 2.17 [1.28, 3.05]% year^{-1} is seen in the observed PAN total columns at Eureka between 2006 and 2020 (Figure 3g). When enhancement events are removed, the slope of the trend at Eureka is largely unchanged with a value of 2.13 [1.64, 2.62]% year^{-1}, however the range of the 95% CIs decreases, indicating a higher confidence in the observed positive trend. At Thule, PAN measurements are only available between 2015 and 2022, and positive but non-significant trends are found, with values of 2.20 [−0.31, 4.61]% year^{-1} with all measurements, and 1.29 [−0.59, 3.22]% year^{-1} when enhancement events are excluded from the time-series (Figure 4g). The magnitude of the slope at Thule is generally consistent with the observations at Eureka, however more years of measurements at the site are likely needed to derive a statistically significant trend.

Relatively few studies are available that report long-term trends in PAN. Bernath et al. (2020) report no statistically significant trend between 2004 and 2012, and then a strongly negative trend of −11.7 ± 2.3% year^{-1} averaged over 60°S to 60°N between 2004 and 2020. Fadnavis et al. (2014) found positive annual PAN trends ranging from 0.4 ± 1.3 to 3.2 ± 0.49 ppt year^{-1} over India, and 1.0 ± 0.25 to 3.4 ± 1.3 ppt year^{-1} over China (no relative trend values provided). Additionally, several studies have demonstrated that PAN production is highly spatially heterogeneous, and that Asian emissions of O_3 and PAN precursors have been steadily rising, leading to increased export of PAN particularly during the springtime (Cooper et al., 2010; Fadnavis et al., 2014; Fischer et al., 2011, 2014; Jiang et al., 2016; L. Zhang et al., 2008). Since Asian anthropogenic emissions are a dominant source of transported pollution at Eureka (Lutsch et al., 2020), the upward trend at Eureka is likely influenced by greater PAN export from Asia in recent decades.

3.3. GEOS-Chem Simulation and Comparison With Observations

Since measurements of CO, C_2H_2, C_2H_6, CH_3OH, HCOOH, H_2CO, and PAN are sparse in the high-Arctic region, global CTMs such as GEOS-Chem can provide an additional perspective on the transport, distribution, and temporal variability and evolution of these trace gases. Ground-based FTIR measurements of these gases can serve as a means for evaluating the performance of the model and can help to identify biases or potential areas of improvement. In the following subsections, we compare the modeled intra- and inter-annual variability of CO, C_2H_2, C_2H_6, CH_3OH, HCOOH, H_2CO, and PAN with the ground-based FTIR measurements at Eureka and Thule.

3.3.1. Seasonal Cycles

The monthly mean simulated total columns from GCHP of all seven tropospheric species are plotted along with the FTIR monthly mean total columns in Figures 5 and 6 for Eureka and Thule, respectively. It should be noted that in Figure 5 the GEOS-Chem time-series was truncated to 2006–2020 before calculating the monthly means to more accurately correspond to the Eureka FTIR time-series, while in Figure 6 the Thule FTIR time-series was truncated to 2003–2021 prior to calculating the monthly means for easier comparison with the GEOS-Chem simulation. Additionally, correlation plots comparing the daily mean simulated total columns with the daily mean FTIR-retrieved total columns at Eureka and Thule are included as Figures S6 and S7 in Supporting Information S1 while the summary statistics of these comparisons are provided in Table 4, providing a more quantitative means of evaluating the model against the FTIR measurements at both sites.

3.3.1.1. CO

The seasonal cycle of CO is well captured by GEOS-Chem at both Arctic FTIR sites, and is shown in Figures 5a and 6a for Eureka and Thule, respectively. The model reflects the observed springtime maximum in February to April and low total columns in July at both sites, with a strong correlation of $R = 0.78$ and a mean relative bias of −5.5% at Eureka, and a correlation coefficient of $R = 0.84$ and mean relative bias of −14.1% at Thule (see Figures S6a and S7a in Supporting Information S1). The closest agreement between the modeled and FTIR-observed

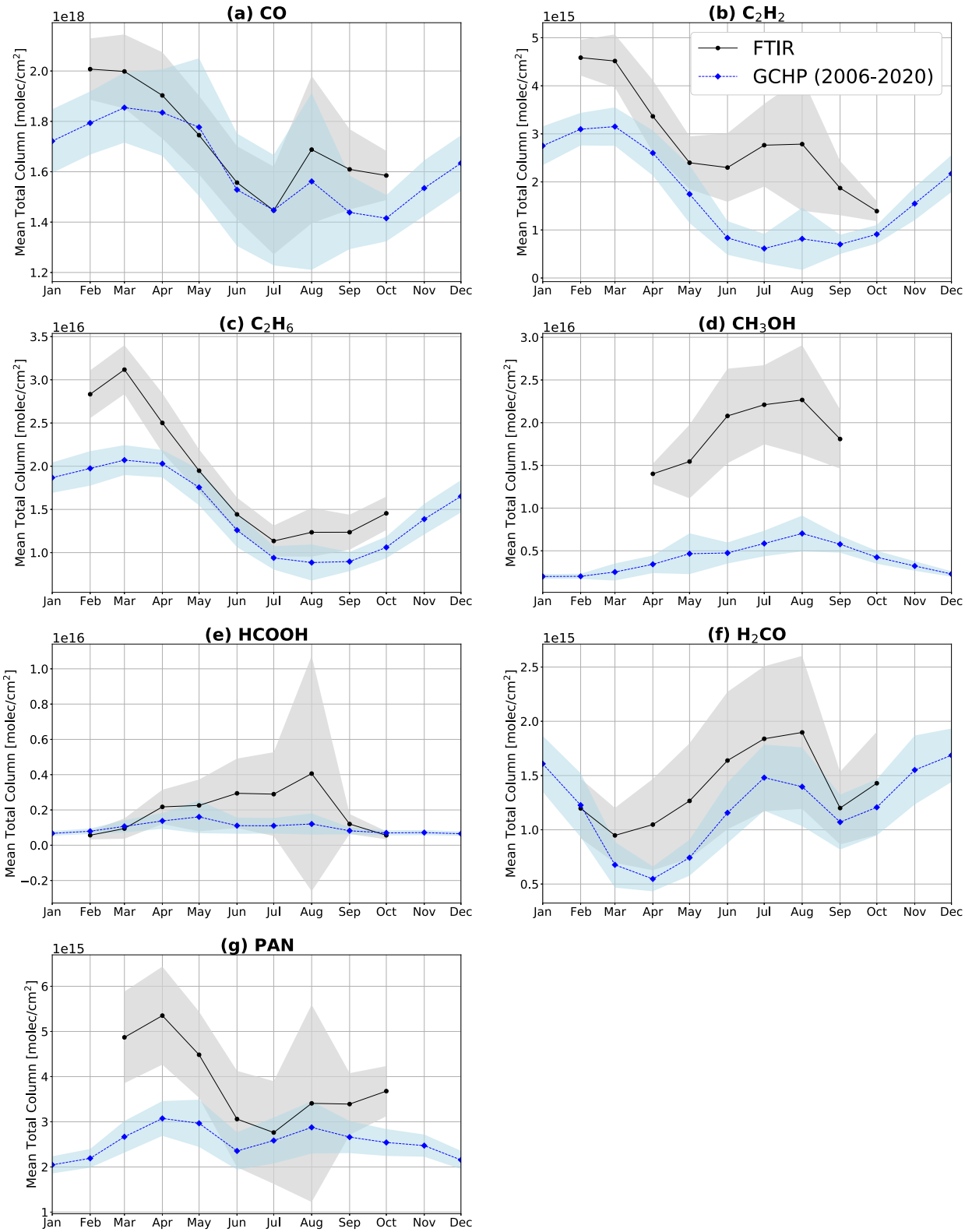

Figure 5. Fourier transform infrared (FTIR) and GEOS-Chem High Performance (GCHP)-simulated seasonal cycles at Eureka for (a) CO, (b) C_2H_2, (c) C_2H_6, (d) CH_3OH, (e) HCOOH, (f) H_2CO, and (g) PAN. The shaded regions denote 1σ from the monthly means. Note that the GCHP monthly means presented here were calculated over 2006–2020 to correspond with the Eureka FTIR time-series.

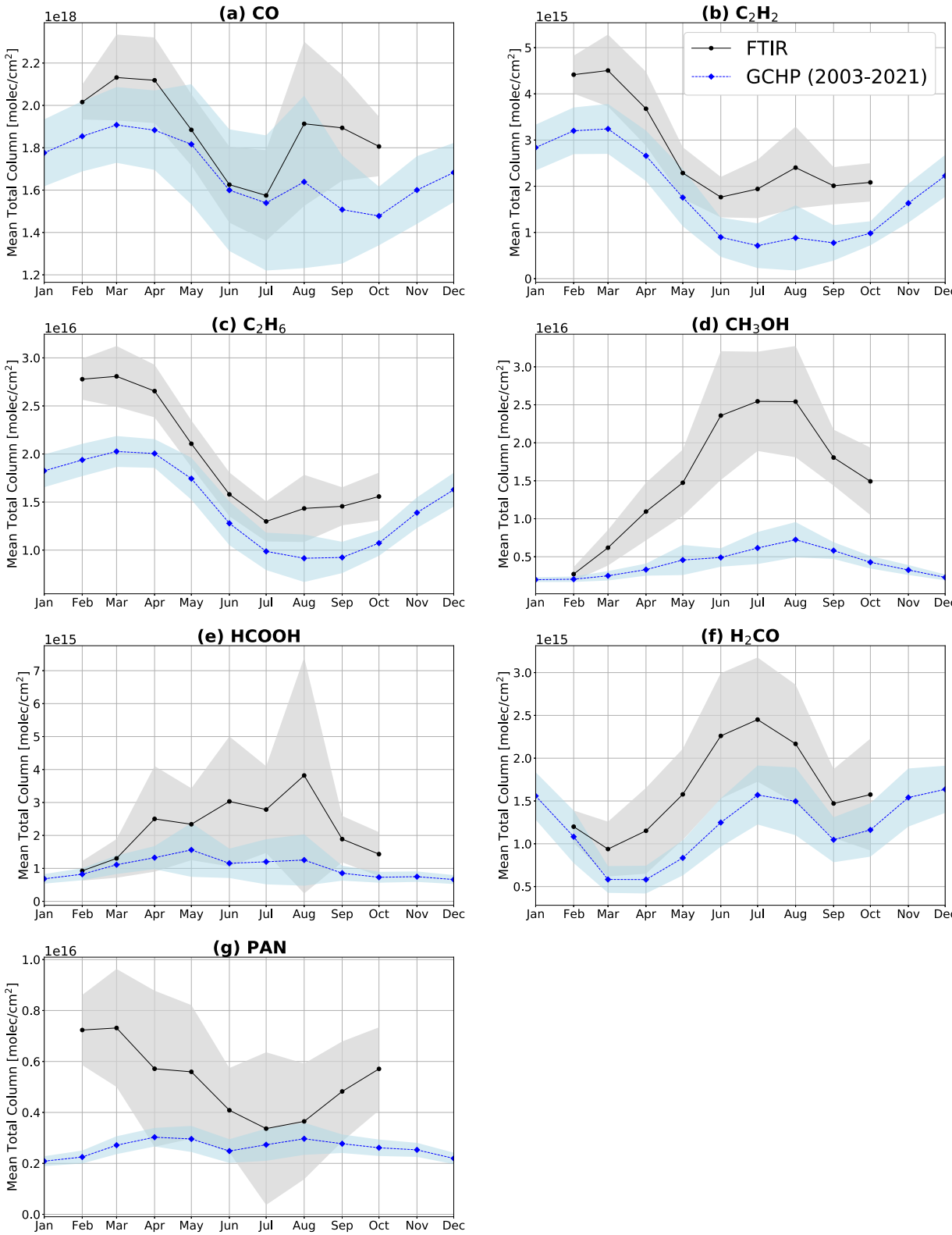

Figure 6. Fourier transform infrared (FTIR) and GEOS-Chem High Performance (GCHP)-simulated seasonal cycles at Thule for (a) CO, (b) C_2H_2, (c) C_2H_6, (d) CH_3OH, (e) HCOOH, (f) H_2CO, and (g) PAN. The shaded regions denote 1σ from the monthly means. Note that the Thule FTIR monthly means presented here were calculated over 2003–2021 to correspond with the time range of the GCHP simulation.

Table 4
The Number of Paired Daily Means (N), Pearson Correlation Coefficients (R), and the Mean Relative Biases Between the Fourier Transform Infrared Measurements and GEOS-Chem at Eureka and Thule

	Eureka, Nunavut (2006–2020)			Thule, Greenland (2003–2021)		
Species	*N*	*R*	μ (%)	*N*	*R*	μ (%)
CO	947	0.78	−5.5	1,467	0.84	−14.1
C_2H_2	770	0.75	−43.4	1,451	0.88	−47.6
C_2H_6	827	0.90	−20.8	1,391	0.91	−25.1
CH_3OH	378	0.28	−70.5	766	0.69	−69.9
HCOOH	860	0.43	−7.9	1,391	0.56	−36.7
H_2CO	965	0.69	−20.5	1,403	0.76	−26.7
PAN	759	0.43	−18.6	460	−0.01	−17.5

mean total columns is seen during the period of May to July, and larger differences are found during the early spring months and the late summer and into early fall. The observed springtime low bias at Eureka and Thule is consistent with previous modeling studies using GEOS-Chem, which have shown that northern mid-latitude CO emissions during the wintertime are broadly underestimated in many anthropogenic emissions inventories due to underestimated vehicle combustion and residential heating emissions (Jiang et al., 2015; Kopacz et al., 2010; Whaley et al., 2022). The GEOS-Chem CO simulation captures biomass burning enhancement events at both Arctic sites in August, however, the magnitude of these enhancements appears to be underestimated in the model, particularly at Thule where a larger measurement-model difference is seen in August compared to Eureka. The observed discrepancy in the simulated versus observed biomass burning enhancements is due in-part to the rudimentary default biomass burning injection height scheme as discussed in Wizenberg, Strong, Jones, Lutsch, et al. (2023), which can negatively impact the transport of the plumes and the subsequent enhancements at the Arctic FTIR sites. However, despite this GEOS-Chem generally performs quite well in simulating the annual CO cycle in the region and is highly correlated with the FTIR observations at Eureka and Thule.

3.3.1.2. C_2H_2

The addition of a full-chemistry simulation of C_2H_2 to the GEOS-Chem model is a relatively recent development (added in version 13.3 in November 2021), and to our knowledge this is the first study to evaluate this simulation against FTIR observations. The monthly mean GEOS-Chem C_2H_2 total columns for Eureka and Thule are shown in Figures 5b and 6b, respectively. The GEOS-Chem simulation displays an intra-annual cycle that is largely consistent with the monthly mean FTIR-observed total columns at both Arctic sites, however a consistent low bias is seen in the model across all months. The modeled C_2H_2 daily-mean total columns display a good correlation of $R = 0.75$ with the FTIR daily-mean total columns at Eureka, however, a mean measurement-model bias of −43.4% was found in the period of 2006–2020 (Figure S6b in Supporting Information S1). Similarly, at Thule the GEOS-Chem C_2H_2 total columns are well-correlated with the FTIR measurements ($R = 0.88$), but a mean negative relative bias of −47.6% was found for the period 2003–2021 (Figure S7b in Supporting Information S1). The strong correlations but large negative model versus measurement biases at both Arctic FTIR sites suggest that the emissions of C_2H_2 in the model should be increased by approximately 40%–50%. Additionally, at Eureka larger biomass burning enhancements of C_2H_2 are observed in comparison to Thule, however, GEOS-Chem shows a relatively small influence of wildfires in the month of August. This effect can also be observed in the correlation plot for Eureka (Figure S6b in Supporting Information S1), where the distribution of the data points displays a bifurcation, and some large daily mean FTIR total columns can be seen that correspond to smaller GEOS-Chem simulated total columns.

3.3.1.3. C_2H_6

The monthly mean model and FTIR C_2H_6 total columns are plotted in Figures 5c and 6c for Eureka and Thule, respectively. GEOS-Chem and the measured total columns generally display a similar seasonal cycle, with a maxima in the total columns occurring in February and March, and a minima in the total columns occurring in July. The simulated C_2H_6 columns are strongly correlated with the FTIR total columns, with correlation coefficients of $R = 0.90$ and $R = 0.91$ and mean relative biases of −20.8% and −25.1% at Eureka and Thule, respectively (see Figures S6c and S7c in Supporting Information S1). A seasonally-dependent bias can be seen at both Arctic sites, with larger mean differences during the early spring months and closer agreement during the late spring and early summer months (May to July). In the default configuration of the model, the Tzompa-Sosa et al. (2017) emissions inventory was selected by the GEOS-Chem Emissions Working Group because the Community Emissions Data System (CEDS) inventory tended to underestimate C_2H_6 emissions in the Northern Hemisphere relative to observations (e.g., Dalsøren et al., 2018). However, a drawback of the Tzompa-Sosa inventory is that it only includes emissions for the year of 2010 (which are subsequently applied to all years in the simulation), and it does not exhibit intra-annual variability in the emissions outside of North America. To

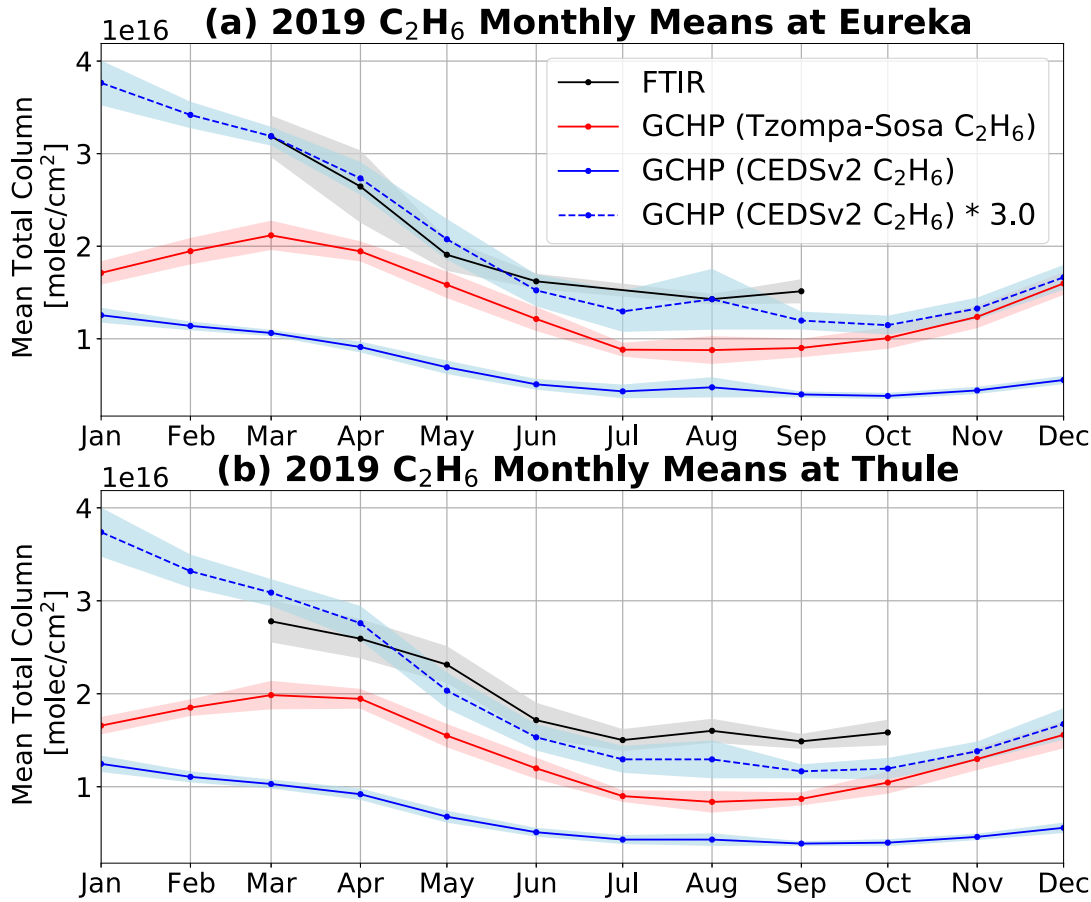

Figure 7. Fourier transform infrared (FTIR) and GEOS-Chem High Performance (GCHP)-simulated monthly mean total columns of C_2H_6 for 2019 at (a) Eureka, and (b) Thule for three scenarios; the default simulation using the Tzompa-Sosa et al. (2017) emissions inventory (red solid line), a simulation using CEDSv2 emissions (blue solid line), and the CEDSv2 simulation with the total columns scaled up by a factor of 3.0 (blue dashed line). The shaded regions denote 1σ from the means.

investigate whether the springtime model bias is related to the choice of anthropogenic emissions, we repeated a GCHP simulation for 2019 using the CEDSv2 C_2H_6 emission inventory in place of the Tzompa-Sosa C_2H_6 inventory, while all other model parameters were kept the same. We compare the monthly means for these simulations in Figure 7, and we provide correlation plots for each scenario for Eureka and Thule in Supporting Information S1 as Figures S8 and S9, respectively. In these figures, we also include an additional scenario whereby the GEOS-Chem C_2H_6 total columns are scaled up by a factor of 3 to account for the observed measurement-model bias. The new simulation using CEDSv2 displays improved correlations of $R = 0.93$ versus $R = 0.88$ and $R = 0.96$ versus $R = 0.94$, but larger biases of -66.6% versus -28.3% and -69.6% versus -34.8% during 2019 at Eureka and Thule, respectively. This observed low bias in the CEDSv2 simulation is consistent with a recent study by Adedeji et al. (2023), who evaluated the CEDS inventory using GEOS-Chem against in-situ measurements on the Japanese island of Hateruma, and found that the Asian C_2H_6 emissions needed to be increased by a factor of 2.22 in order to reproduce their observations. Similar low biases have also previously been observed in the Hemispheric Transport of Air Pollutants, Phase II (HTAPv2) inventory using CAM-Chem simulations in Franco et al. (2016a). In Figure 7 and Figures S8c and S9c in Supporting Information S1, we show that when the modeled C_2H_6 total columns in our simulation using CEDSv2 are increased by a factor of 3.0, we find improved slopes in the linear regressions and much closer agreement with the FTIR measurements at Eureka and Thule. Although this is only an ad hoc analysis, it indicates that by using a scaled version of the CEDSv2 C_2H_6 emissions in place of the default Tzompa-Sosa inventory, the simulation could be improved relative to observations and would better capture the intra-annual variability of C_2H_6 in the Arctic region.

3.3.1.4. CH_3OH

Figures 5d and 6d show the monthly mean simulated and observed CH_3OH total columns at Eureka and Thule, respectively. The GEOS-Chem total columns display a seasonal cycle similar to the FTIR observations, with smaller columns on average during the spring and fall, and larger columns during the summer months of July to September, however a very large bias can be seen at both Arctic sites. Regression plots comparing the GEOS-Chem and FTIR CH_3OH daily-means are shown in Figure S6d in Supporting Information S1 for Eureka and Figure S7d in Supporting Information S1 for Thule. Consistent negative biases relative to the FTIR measurements on the order of approximately −70% are found at both Eureka and Thule, suggesting that there may be a large source of CH_3OH or unknown chemical pathways which are not accounted for in the model. We find a relatively weak correlation of $R = 0.28$ between the model and measurements at Eureka, but a stronger correlation of $R = 0.69$ at Thule, which is related to the fact that the FTIR CH_3OH measurements at Thule cover a larger portion of the year (February to October at Thule, and April to September at Eureka) and exhibit a higher dynamic range than at Eureka. The observed model bias in CH_3OH is generally consistent with recent GEOS-Chem modeling studies by Bates et al. (2021) and Chen et al. (2019), who found that the modeled CH_3OH concentrations over North America are broadly underestimated relative to observations, with the largest biases at high latitudes. Improvements were made to the CH_3OH simulation in GEOS-Chem version 13.3.0 in November 2021 through the addition of a new aromatic VOC oxidation scheme and the inclusion of a $CH_3O_2 + OH$ reaction into the chemistry scheme, which generally reduced the observed biases, however, it is evident that more improvements are needed to remediate the large measurement-model biases in the Arctic.

3.3.1.5. HCOOH

The modeled and observed seasonal cycles of HCOOH are shown in Figures 5e and 6e for Eureka and Thule, respectively. The GEOS-Chem simulation displays seasonality which is mostly consistent with the FTIR observations at both sites, with smaller mean columns during early and late in the year, and larger columns on average during the late spring and summer. However, the model presents a maximum in May, while the FTIR measurements show a peak in August that is related to the large wildfire enhancements that can occur during the mid to late summer, but which may not be properly captured in the model due to the injection height scheme. Correlation plots comparing the daily mean GEOS-Chem HCOOH total columns and the FTIR daily means are shown in Figures S6e and S7e in Supporting Information S1. These figures show moderate correlations of $R = 0.43$ and $R = 0.53$ between the model and measurements, with mean relative biases of −7.9% and −36.7% at Eureka and Thule, respectively. The observed biases are generally in-line with previous comparisons of models with observations that found underestimations in HCOOH abundances, particularly at high northern latitudes, suggesting missing chemistry or unknown local sources (Paulot et al., 2011; Schobesberger et al., 2016; Stavrakou et al., 2012). The inclusion of a surface-level source of HCOOH in the Arctic from the snow-pack based on the observations of Mungall et al. (2018) may help bridge the gap of the observed biases in the late spring to some extent, however the nature of this local source of HCOOH is still highly uncertain and requires further investigation. Furthermore, an improved parameterization of the biomass burning injection height in the model would help to improve agreement with observations in the late summer months as demonstrated in Wizenberg, Strong, Jones, Lutsch, et al. (2023).

3.3.1.6. H_2CO

Figures 5f and 6f show the simulated and observed H_2CO monthly means at Eureka and Thule, respectively. GEOS-Chem is able to reproduce the distinct seasonality in the total columns observed by the FTIRs at both sites, and shows the largest total columns occurring during the winter months of November to January, however no FTIR measurements are available during this period for comparison. The simulated H_2CO columns reach a minimum at both sites in April and then increase until July before decreasing again, which is generally consistent with the observed seasonal cycle at Eureka and Thule but a low model bias can be seen across all months relative to the FTIR monthly means. The correlations between the daily-mean GEOS-Chem and FTIR H_2CO total columns are shown in Figure S6f in Supporting Information S1 for Eureka and Figure S7f in Supporting Information S1 for Thule. The GEOS-Chem columns are generally well-correlated with the FTIR observations, with a correlation coefficient of $R = 0.69$ at Eureka, and $R = 0.76$ at Thule. Moderate relative biases of −20.5% and −26.7% calculated across all years were found for Eureka and Thule, respectively. These mean biases are

Table 5
Fitted Trends Derived From Daily-Mean GEOS-Chem Total Columns at Eureka and Thule in Relative Units (% year^{-1})

	Eureka, Nunavut (2006–2020)		Thule, Greenland (2003–2021)	
Species	Trend (% year^{-1})	Trend w/o enhancements (% year^{-1})	Trend (% year^{-1})	Trend w/o enhancements (% year^{-1})
CO	**−0.88** (−1.09, −0.67)	**−0.85** (−0.98, −0.72)	**−0.79** (−0.98, −0.61)	**−0.86** (−0.94, −0.77)
C_2H_2	**−2.03** (−2.46, −1.61)	**−1.95** (−2.22, −1.68)	**−1.63** (−1.91, −1.35)	**−1.71** (−1.85, −1.55)
C_2H_6	−0.19 (−0.38, 0.01)	**−0.16** (−0.27, −0.05)	**−0.26** (−0.42, −0.11)	**−0.28** (−0.34, −0.21)
CH_3OH	−0.45 (−0.90, 0.02)	**−0.43** (−0.63, −0.24)	−0.24 (−0.52, 0.05)	**−0.20** (−0.33, −0.07)
HCOOH	**−1.17** (−1.97, −0.36)	**−1.09** (−1.41, −0.77)	**−0.71** (−1.11, −0.32)	**−0.59** (−0.78, −0.41)
H_2CO	−0.18 (−0.47, 0.13)	−0.13 (−0.29, 0.03)	0.08 (−0.16, 0.16)	0.02 (−0.11, 0.16)
PAN	**−0.80** (−1.00, −0.60)	**−0.83** (−0.94, −0.71)	**−0.61** (−0.75, −0.48)	**−0.58** (−0.66, −0.50)

Note. The 95% confidence intervals calculated from bootstrap resampling with $Q = 5{,}000$ ensemble members are provided below each value in parentheses. Trends that are considered statistically significant (i.e., the 95% confidence intervals do not overlap with zero) are in bold.

consistent with the study by Vigouroux et al. (2018), who found similar measurement-model biases of −20% and −28% with the IMAGES CTM at Eureka and Thule in the periods of 2006–2017 and 2002–2017, respectively.

3.3.1.7. PAN

The simulated and observed monthly mean PAN total columns are shown in Figure 5g at Eureka and Figure 6g at Thule. GEOS-Chem does capture some seasonal cycle, with the lowest mean total columns in December and January, and a springtime peak in April, with some large columns occurring in August as the result of transported wildfire plumes. However, a very large negative bias in the model can be seen from February to May. Correlation plots comparing the GEOS-Chem daily mean PAN columns with those retrieved from the Arctic FTIRs are shown in Figures S6g and S7g in Supporting Information S1. A moderate correlation of $R = 0.43$ is found at Eureka, while no correlation ($R = -0.01$) is found at Thule, however the comparison at Thule covers a shorter time period (2015–2021) compared to Eureka (2007–2020). Mean relative biases of −18.6% and −17.5% were found for Eureka and Thule, respectively, indicating a similar underestimation in the model at both Arctic sites. The observed springtime bias in the total columns is likely related to lower than expected wintertime outflows of PAN from China, which is attributed partly to missing or underestimated NMVOC emissions in the region as highlighted in the studies by Fischer et al. (2014) and Fu et al. (2007). Increasing Asian NMVOC emissions in the model would likely enhance the simulation of PAN in the Arctic region and reduce the mean differences relative to the FTIR observations.

3.4. Simulated Trends

To further evaluate the performance of the model and its ability to reproduce the observed trends, the Fourier series fitting approach that was described in Section 2.3 and applied to the FTIR daily-mean total columns in Section 3.2 was also applied to the GEOS-Chem simulated daily mean total columns. To increase the intercomparability of the observed and modeled trends, the GCHP-simulated trends at Eureka were calculated over the same approximate time range as where the Eureka FTIR measurements are available (July 2006 to March 2020). At Thule, since the FTIR time-series extends slightly beyond the time range of the GCHP simulation, we calculate the GCHP-simulated trends over the full simulation period (January 2003 to December 2021). The daily-mean simulated total columns of all species at each site, and the fitted trends and 95% CIs in% year^{-1} are summarized in Table 5, and are plotted in Figures 8 and 9 for Eureka and Thule, respectively. A version of Table 5 in total column units is included in Supporting Information S1 as Table S2.

3.4.1. CO

The fitted trends in the GEOS-Chem simulated CO columns are shown in Figures 8a and 9a for Eureka and Thule, respectively. From GEOS-Chem, we obtain a negative trend in the CO total columns of −0.88 [−1.09, −0.67]% year^{-1} at Eureka between 2006 and 2020, and −0.79 [−0.98, −0.61]% year^{-1} at Thule between 2003 and 2021. When enhancement events are excluded from the Fourier series fit, we find a slightly less negative trend

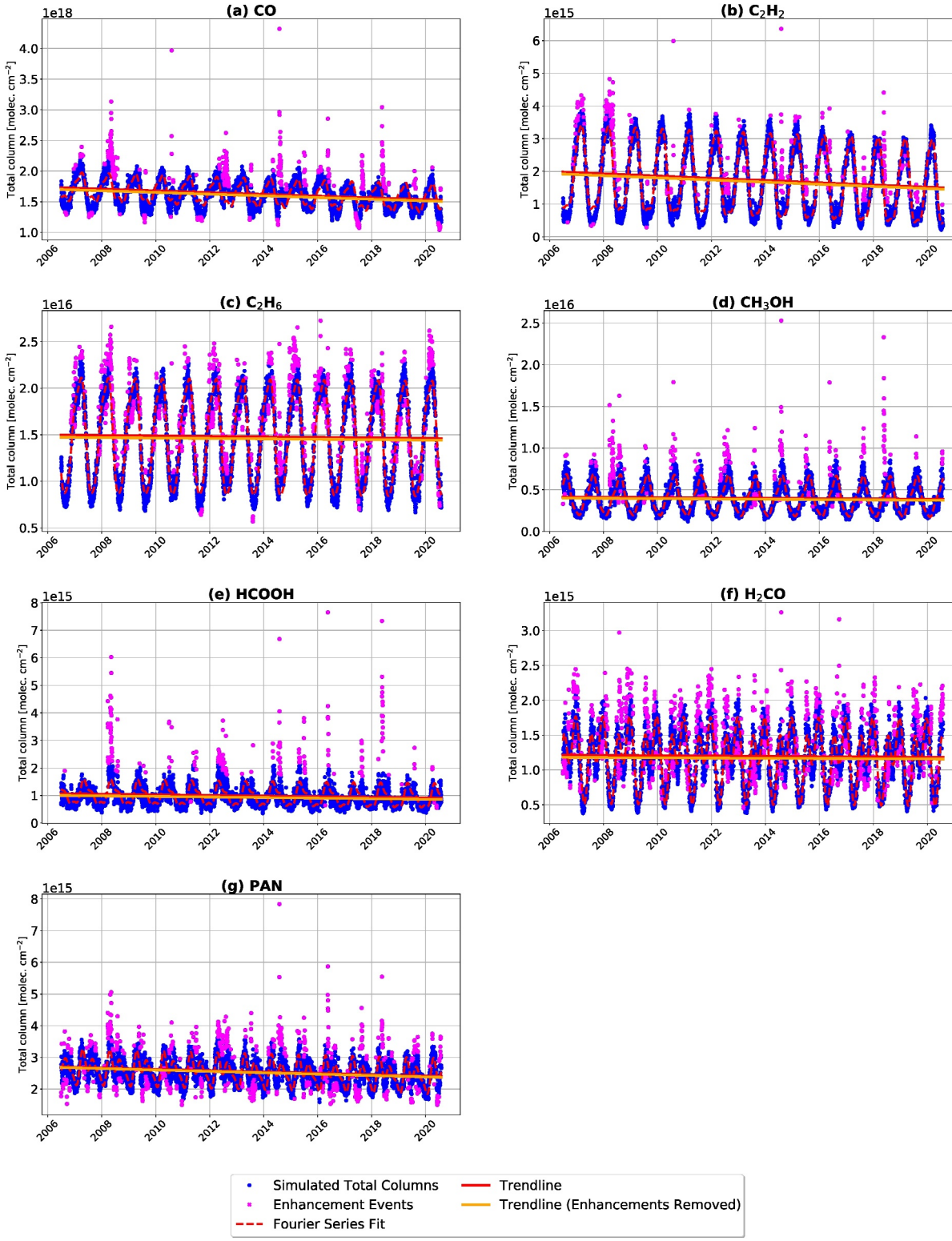

Figure 8. Fourier series fit and the corresponding trendlines plotted over the GEOS-Chem High Performance (GCHP) simulated total column time-series of (a) CO, (b) C_2H_2, (c) C_2H_6, (d) CH_3OH, (e) HCOOH, (f) H_2CO, and (g) PAN at Eureka.

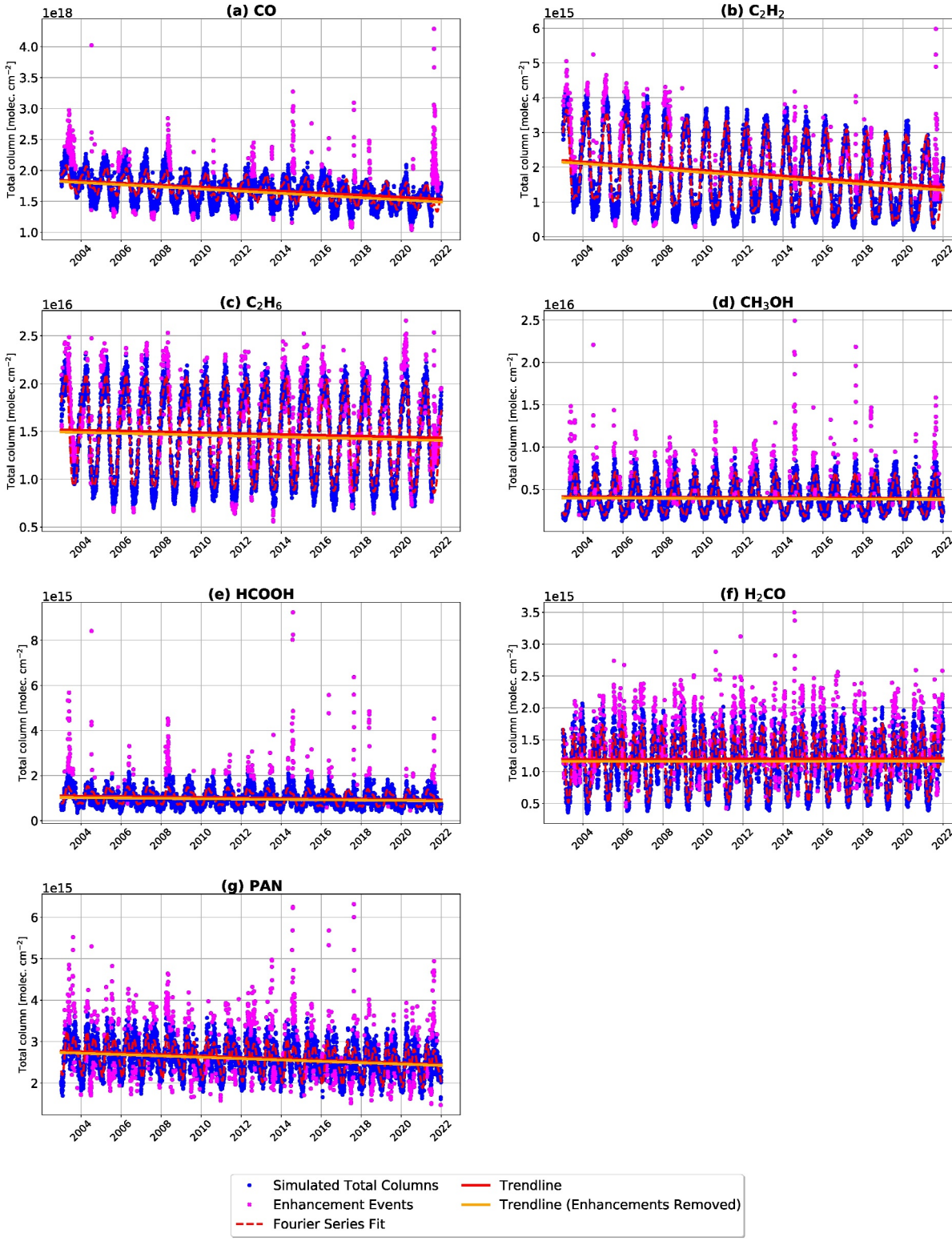

Figure 9. Fourier series fit and the corresponding trendlines plotted over the GEOS-Chem High Performance (GCHP) simulated total column time-series of (a) CO, (b) C_2H_2, (c) C_2H_6, (d) CH_3OH, (e) HCOOH, (f) H_2CO, and (g) PAN at Thule.

at Eureka of −0.85 [−0.98, −0.72]% year^{-1}, and a slightly more negative trend at Thule of −0.86 [−0.94, −0.77]% year^{-1}. This effect appears to be caused by the fact that some larger enhancement events occur earlier in the simulation at Eureka, while at Thule, the largest identified enhancements occur toward the end of the simulated time-series. These trends can be contrasted with the FTIR-derived trends of −0.84 [−1.07, −0.62] and −0.76 [−0.94, −0.58] (with enhancements), and −1.10 [−1.23, −0.97] and −0.89 [−0.99, −0.79] (without enhancements) at Eureka and Thule, respectively. The measured and modeled trends are broadly consistent, and fall within the bounds of the 95% CIs with the exception of the enhancement-removed FTIR-derived trend at Eureka which is more strongly negative than that estimated from GEOS-Chem. In general, CO appears to be well-modeled in GCHP at both Arctic FTIR sites, showing good consistency in the inter-annual variability when compared with the FTIR observations.

3.4.2. C_2H_2

For C_2H_2, we derive negative trends from the daily-mean GEOS-Chem total columns of −2.03 [−2.46, −1.95]% year^{-1} at Eureka (Figure 8b), and −1.63 [−1.91, −1.35]% year^{-1} at Thule (Figure 9b). If enhancement events are removed, we obtain a slightly less negative trend of −1.95 [−2.22, −1.68]% year^{-1} at Eureka, and −1.71 [−1.85, −1.55]% year^{-1} at Thule. The tendency of the C_2H_2 trend to become more strongly negative at Thule when removing the identified enhancement events is consistent with the modeled CO trends at this site, and appears to be influenced by a particularly large wildfire enhancement that occurred in August 2021 but which is not included when fitting the trends at Eureka. We can compare these modeled trends with the FTIR-derived trends of −2.20 [−3.03, −1.34]% year^{-1} and −1.71 [−2.03, −1.38]% year^{-1} when all measurements are included, and −2.57 [−3.14, −1.96]% year^{-1} and −1.61 [−1.83, −1.39]% year^{-1} when enhancements are removed for Eureka and Thule, respectively. Consistent with the modeled CO trends, we find that there is generally good agreement between the FTIR-derived and GEOS-Chem simulated C_2H_2 trends at both sites, with all trends overlapping within the bounds of the 95% CIs except for the enhancement-removed trend at Eureka, which is more strongly negative than the GEOS-Chem derived trend.

3.4.3. C_2H_6

The Fourier series fits to the GEOS-Chem C_2H_6 daily-mean total columns are shown in Figures 8c and 9c for Eureka and Thule, respectively. We find no significant trend at Eureka when fitting the full simulated time-series with a slope of −0.19 [−0.38, 0.01]% year^{-1}, but a small negative trend when enhancements are removed of −0.16 [−0.27, −0.05]% year^{-1}. At Thule, slight negative trends are also found in the GEOS-Chem C_2H_6 time-series with values of −0.26 [−0.42, −0.11]% year^{-1} with all data and −0.28 [−0.34, −0.21]% year^{-1} when enhancements are removed. These simulated trends can be contrasted with the positive trends derived from the Arctic FTIR measurements of 1.07 [0.76, 1.38]% year^{-1} and 0.61 [0.39, 0.84]% year^{-1} (all data), and 0.98 [0.77, 1.18]% year^{-1} and 0.56 [0.42, 0.70]% year^{-1} (enhancements excluded) at Eureka and Thule, respectively. The difference in the observed versus modeled trends is likely due in part to the use of the Tzompa-Sosa et al. (2017) emissions inventory which is the default option for the anthropogenic C_2H_6 emissions in the current version of GEOS-Chem. As briefly discussed in Section 3.3.1, the Tzompa-Sosa emissions inventory only contains data for the year of 2010, which is applied to all years in the simulation, and thus does not exhibit any inter-annual variability in the global C_2H_6 emissions. To further investigate the long-term temporal variability in the Tzompa-Sosa and CEDSv2 C_2H_6 inventories, the HEMCO Standalone module (https://hemco.readthedocs.io/en/stable/) version 3.6.2 was used to generate the time-series of emissions over the same period as the GCHP simulation (2003–2021). Time-series of C_2H_6 emissions over Asia and North America using both the Tzompa-Sosa and CEDSv2 emissions inventories are shown in Figure S10 in Supporting Information S1. When comparing the time-series from the two inventories, a clear discrepancy can be seen in the magnitude of the emissions, with CEDSv2 being significantly lower than the Tzompa-Sosa inventory in both regions. However, while there is seasonality in the Tzompa-Sosa emissions over North America, there is no seasonal variability in the emissions over Asia (and all other regions) and they are constant throughout the simulation period. In addition, the Tzompa-Sosa inventory shows no inter-annual variability in the emissions, while with the CEDSv2 inventory there is a clear evolution of the emissions over the period of 2003–2021. As a simple ad hoc solution to reconcile the differences between these two inventories, we suggest that the CEDSv2 emissions time-series be scaled up to match the magnitude of the Tzompa-Sosa emissions during the year of 2010, with the scaling factors being calculated on a by-region basis. This could yield an inventory that better captures both the magnitude and the

temporal variability of the emissions, and would improve the simulation of C_2H_6 in the model relative to observations.

3.4.4. CH_3OH

For CH_3OH, no statistically significant trends are found when fitting the full time-series of GEOS-Chem daily-mean total columns, with slopes of −0.45 [−0.90, 0.01]% year^{-1} at Eureka (Figure 8d) and −0.24 [−0.52, 0.05]% year^{-1} at Thule (Figure 9d). When enhancements are excluded from the fit, we find small but statistically significant negative trends at both locations with values of −0.43 [−0.63, −0.24]% year^{-1} and −0.20 [−0.33, −0.07]% year^{-1} at Eureka and Thule, respectively. At Eureka, no statistically significant trend was detected in the FTIR time-series when all data were fitted, but a negative trend on the order of −0.57 [−1.07, −0.08]% year^{-1} was found for the period of 2007–2019 when enhancement events were removed from the time-series. At Thule, statistically significant negative trends were found in both cases with relative values of −2.02 [−2.73, −1.30]% year^{-1} (all measurements) and −1.64 [−2.09, −1.20]% year^{-1} (enhancements excluded). There is general consistency in the direction of the observed and modeled CH_3OH trends, and the enhancement-removed GEOS-Chem trend at Eureka falls within the range of the 95% CIs of the fitted FTIR trend, but the FTIR-derived trend at Thule is more strongly negative than the one derived from GEOS-Chem and the CIs do not overlap. Further study is required to identify the source of the negative CH_3OH trends in the Arctic region.

3.4.5. HCOOH

Statistically significant negative trends in the modeled daily-mean total columns of HCOOH were found at Eureka and Thule with values of −1.17 [−1.97, −0.36]% year^{-1} and −0.71 [−1.11, −0.32]% year^{-1}, respectively (shown in Figures 8e and 9e). If enhancement events are excluded from the GEOS-Chem time-series, we obtain slightly less negative trends of −1.09 [−1.41, −0.77]% year^{-1} and −0.59 [−0.78, −0.41]% year^{-1}. From the FTIR data sets, a trend of −2.98 [−4.13, −1.82]% year^{-1} was found at Eureka between 2006 and 2020 when enhancements were excluded from the Fourier series fit, but no statistically significant trends were found when fitting the full Eureka time-series, and at Thule with or without enhancements. The negative trends simulated by GEOS-Chem appear to be driven by broad reductions in Northern Hemisphere anthropogenic emissions of HCOOH between 2003 and 2021, particularly in North America and Asia, which is shown in Figure S11 in Supporting Information S1. The values of the fitted slopes from GEOS-Chem fall in between the negative trends reported by Yamanouchi et al. (2021) (−2.15 ± 0.64% year^{-1}) at Toronto and Bernath et al. (2020) (−0.51 ± 0.28% year^{-1}) in the range of 60°S to 60°N.

3.4.6. H_2CO

No statistically significant trends could be derived from the GEOS-Chem simulated H_2CO total columns at either Arctic FTIR site (Figures 8f and 9f). At Eureka, a slope of −0.18 [−0.47, 0.13]% year^{-1} when all data are included in the Fourier series fit, and −0.13 [−0.29, 0.03]% year^{-1} when enhancements are excluded from the fit. At Thule, we find slopes of 0.08 [−0.16, 0.16]% year^{-1} with all data, and 0.02 [−0.11, 0.16]% year^{-1} without enhancement events. In comparison, statistically significant positive trends were derived from the FTIR measurements at both Arctic sites, with values at Eureka of 2.02 [1.20, 2.84]% year^{-1} (all measurements) and 1.91 [1.42, 2.40]% year^{-1} (enhancements removed), and 1.19 [0.66, 1.72]% year^{-1} (all measurements) and 0.97 [0.65, 1.29]% year^{-1} (enhancements removed) at Thule. To investigate whether increasing CH_4 concentrations have an influence on the simulated H_2CO columns in the Arctic, we repeated the Fourier series fitting on the modeled H_2CO partial columns at both sites. We apply separate Fourier fits to the lower troposphere (defined here as the surface to the model planetary boundary layer), free troposphere (planetary boundary layer to the model tropopause), the whole troposphere (surface to tropopause), as well as the stratosphere to the top of the atmosphere (tropopause to the top of the model grid) where the formation of H_2CO via CH_4 oxidation is expected to play the largest role. The fits to the partial columns are shown in Figures S12 and S13 in Supporting Information S1 for Eureka and Thule, respectively. At Eureka, we find no statistically significant trends in the simulated H_2CO partial columns in the troposphere, but a negative trend on the order of −0.69 [−1.00, −0.38]% year^{-1} in the stratospheric partial columns (enhancements excluded). At Thule, we observe a negative trend in the lower troposphere of −0.66 [−0.86, −0.46]% year^{-1}, a slight positive trend in the free troposphere of 0.23 [0.05, 0.40]% year^{-1}, and a negative trend in the stratosphere of −0.23 [−0.44, −0.02]% year^{-1}, but no trend when fitting the full-troposphere partial columns. The presence of negative H_2CO trends in the stratosphere of the model at both Arctic sites is

surprising because the modeled CH_4 total columns were found to be steadily increasing by 0.36 [0.347, 0.368]% year^{-1} and 0.32 [0.316, 0.331]% year^{-1} at Eureka and Thule, respectively (not shown). The source of the observed downward trend in H_2CO in the stratosphere of the model is currently unclear.

3.4.7. PAN

The simulated PAN daily-mean total columns are plotted along with the fitted trendlines in Figures 8g and 9g and show statistically significant negative trends at both Arctic FTIR sites. At Eureka, we obtain trends of −0.80 [−1.00, −0.60]% year^{-1} (-2.12×10^{13} [-2.66×10^{13}, -1.59×10^{13}] molec. cm^{-2} year^{-1}) when all data are included, and −0.83 [−0.94, −0.71]% year^{-1} (-2.19×10^{13} [-2.50×10^{13}, -1.88×10^{13}] molec. cm^{-2} year^{-1}) when enhancements are excluded for the period of 2006–2020. At Thule, we derive trends from GEOS-Chem of −0.61 [−0.75, −0.48]% year^{-1} (-1.72×10^{13} [-2.10×10^{13}, -1.35×10^{13}] molec. cm^{-2} year^{-1}) and −0.58 [−0.66, −0.50]% year^{-1} (-1.64×10^{13} [-1.87×10^{12}, -1.41×10^{13}] molec. cm^{-2} year^{-1}) between 2003 and 2021 for all data and the enhancement-removed cases, respectively. These simulated trends are in disagreement with the positive trends derived from the FTIR at Eureka of 2.17 [1.28, 3.05]% year^{-1} (all data) and 2.13 [1.64, 2.62]% year^{-1} (enhancements excluded). As discussed earlier, this discrepancy between the modeled and observed trend in PAN can most likely be attributed to missing or underestimated emissions of precursor NMVOCs in Asia, as well as the absence of direct emissions of methylglyoxal in the model which is an substantial source of PAN in the global budget (Fischer et al., 2014; Fu et al., 2007).

4. Conclusions

We have presented the first long-term study of the trends and seasonal variability of seven tropospheric pollutant species: CO, C_2H_2, C_2H_6, CH_3OH, HCOOH, H_2CO, and PAN in the North American high-Arctic region. The intra- and inter-annual variability of these seven trace gases was derived from the total column time-series measured by two high-resolution ground-based FTIR instruments located at Eureka, Nunavut (2006–2020) and Thule, Greenland (1999–2022). Strong consistency in the measured seasonal cycles was found across the two sites for all gases, and the influence of transported mid-latitude biomass burning plumes was observed to varying degrees in the time-series of all gases at Eureka and Thule. Negative trends consistent with past studies were found for CO and C_2H_2 with relative values of −1.10 [−1.23, −0.97]% year^{-1} and −2.57 [−3.14, −1.96]% year^{-1} at Eureka, and −0.89 [−0.99, −0.79]% year^{-1} and −1.61 [−1.83, −1.39]% year^{-1} at Thule, respectively (enhancement-excluded trends). Negative trends were also observed in the measured CH_3OH total columns with slopes of −0.57 [−1.07, −0.08]% year^{-1} at Eureka and −1.64 [−2.09, −1.20]% year^{-1} at Thule. A negative trend in HCOOH was found at Eureka of −2.98 [−4.13, −1.82]% year^{-1} when enhancements were excluded, but no trend was observed at Thule. Positive trends were detected for C_2H_6 and H_2CO of 0.98 [0.77, 1.18]% year^{-1} and 1.91 [1.42, 2.40]% year^{-1} at Eureka, and 0.61 [0.39, 0.84]% year^{-1} and 0.97 [0.65, 1.29]% year^{-1} at Thule, respectively. A positive trend in PAN of 2.13 [1.64, 2.62]% year^{-1} was also detected in the Eureka time-series, while at Thule the time-series of PAN only spans the period of 2015–2022 and was too short to reliably discern a trend.

To provide an additional point of comparison and to assess the performance of the novel GCHP CTM in this high-latitude region, a global C48 simulation covering the period of 2003–2021 was performed using version 14.1.1 of the model. We evaluated the simulated intra- and inter-annual variability against the FTIR-derived seasonal cycles and trends at Eureka and Thule. GEOS-Chem was generally able to reproduce the shape of the FTIR-observed seasonal cycles, however significant measurement-model biases exist for some species, with the concentrations of all gases being biased low on average relative to the Arctic FTIRs. GCHP CO, C_2H_2, C_2H_6, and H_2CO were found to be well-correlated with the FTIR observations and with relative biases ranging from −5.5% (CO at Eureka) to −47.6% (C_2H_2 at Thule). GCHP HCOOH was moderately correlated with FTIR observations at both sites, with mean biases of −36.7% and −7.9% at Eureka and Thule, respectively. GCHP PAN shows poor agreement with the FTIR at Thule, but improved agreement at Eureka which may be attributed to the shorter time-series of these species at Thule (2015–2022 vs. 2006–2020 at Eureka). GCHP CH_3OH was found to have a very large bias on the order of −70% relative to the FTIR measurements at both Eureka and Thule, possibly indicating missing local sources or unknown chemistry that are not accounted for in the model. The modeled trends showed broad consistency with those derived from the FTIRs for CO (modeled trends of −0.85% year^{-1} at Eureka, and −0.86% year^{-1} at Thule), C_2H_2 (Eureka: −1.95% year^{-1}, Thule: −1.71% year^{-1}), and CH_3OH (Eureka: −0.43% year^{-1}, Thule: −0.20% year^{-1}). However, opposing trends in the model relative to the FTIRs were found for C_2H_6 (Eureka: −0.16% year^{-1}, Thule: −0.28% year^{-1}) and PAN (Eureka: −0.83% year^{-1}, Thule:

−0.58% year^{-1}), and no trend was found in the modeled H_2CO columns despite positive trends being observed in the FTIR data sets at both sites. While other forms of model errors (i.e., due to transport, chemistry or numerical diffusion) can not be excluded as general contributing factors, for some species the observed discrepancies between the measured and modeled trends can be attributed to errors or underestimations in the model's emissions inventories. In particular, the default configuration of the model uses the Tzompa-Sosa et al. (2017) inventory for C_2H_6 but it only contains emissions for the year of 2010 and does not exhibit seasonality in the emissions outside of North America, resulting in large springtime biases at the Arctic sites and trends which disagree with observations. Future focused studies to better identify the sources of the measurement-model differences presented here, particularly for C_2H_2, CH_3OH, H_2CO, and PAN, could be highly valuable for improving the modeling of these species at these high latitudes.

Continued monitoring of the Arctic atmosphere is critical, particularly in the face of anthropogenic climate change which has already begun to influence pollution sources and transport patterns. The trends and seasonal cycles derived from ground-based FTIRs such as those used in this study are valuable for evaluating the impacts of both natural and anthropogenic emissions on the sensitive Arctic atmosphere, and they are indispensable for the validation of CTMs in this sparsely measured region of the globe. The long-term FTIR measurement programs at Eureka (2006–2020) and Thule (1999–2022) have enabled the quantification of the trends and seasonality of seven tropospheric pollutants in the North American high-Arctic region, and efforts should be focused on the continuation of these time-series.

Data Availability Statement

Version 14.1.1 of the GEOS-Chem High Performance model (GEOS-Chem, 2023) was used in this work, and is freely available to the public via https://doi.org/10.5281/zenodo.7600586. A description of the model and configuration used in this study is provided in the text. The authors acknowledge the use of the GFASv1.2 emissions inventory, which contains modified Copernicus Atmosphere Monitoring Service information (2018). The Eureka and Thule FTIR CO, C_2H_2, C_2H_6, CH_3OH, HCOOH, H_2CO, and PAN data are available on the Borealis Canadian Dataverse Repository (Wizenberg, Strong, Jones, Hannigan, et al., 2023) which is accessible at https://doi.org/10.5683/SP3/CSGZBA.

Acknowledgments

Bruker FTIR measurements were made at PEARL by the Canadian Network for the Detection of Atmospheric Composition Change (CANDAC), which has been supported by the Atlantic Innovation Fund/Nova Scotia Research Innovation Trust, Canada Foundation for Innovation, Canadian Foundation for Climate and Atmospheric Sciences, Canadian Space Agency, Environment and Climate Change Canada (ECCC), Government of Canada International Polar Year funding, Natural Sciences and Engineering Research Council, Northern Scientific Training Program, Ontario Innovation Trust, Polar Continental Shelf Program, and Ontario Research Fund. We thank former CANDAC/PEARL/PAHA PI James Drummond, Canadian Arctic ACE/OSIRIS Validation Campaign PI Kaley Walker, PEARL Site Manager Pierre Fogal, CANDAC Data Manager Yan Tsehtik, the CANDAC operators, and the staff at ECCC's Eureka Weather Station for their contributions to data acquisition, and for logistical and on-site support. The National Center for Atmospheric Research is sponsored by the National Science Foundation. The NCAR FTIR observation program at Thule, Greenland is supported under contract by the National Aeronautics and Space Administration (NASA). The Thule work is also supported by the NSF Office of Polar Programs (OPP) and Battelle ARO. We wish to thank the Danish Meteorological Institute for support at the Thule site. We also thank Dr G. C. Toon (Jet Propulsion Laboratory, California Institute of Technology, Pasadena, CA) for generating and making available the pseudo-linelists as well as the ATM20 line-by-line compilation. The MERRA-2 and GEOS-FP meteorological fields used in the GEOS-Chem simulations in this work were provided by NASA/GMAO. Computations were performed on the Niagara supercomputer at the SciNet HPC Consortium. SciNet is funded by Innovation, Science and Economic Development Canada, the Digital Research Alliance of Canada, the Ontario Research Fund—Research Excellence, and the University of Toronto. E. Mahieu is a Senior Research Associate supported by the Belgian F.R.S.-FNRS.

References

Adedeji, A. R., Andrews, S. J., Rowlinson, M. J., Evans, M. J., Lewis, A. C., Hashimoto, S., et al. (2023). Measurement report: Assessment of Asian emissions of ethane and propane with a chemistry transport model based on observations from the island of Hateruma. *Atmospheric Chemistry and Physics*, *23*(16), 9229–9244. https://doi.org/10.5194/acp-23-9229-2023

Akagi, S. K., Yokelson, R. J., Wiedinmyer, C., Alvarado, M. J., Reid, J. S., Karl, T., et al. (2011). Emission factors for open and domestic biomass burning for use in atmospheric models. *Atmospheric Chemistry and Physics*, *11*(9), 4039–4072. https://doi.org/10.5194/acp-11-4039-2011

Alvarado, M. J., Logan, J. A., Mao, J., Apel, E., Riemer, D., Blake, D., et al. (2010). Nitrogen oxides and PAN in plumes from boreal fires during ARCTAS-B and their impact on ozone: An integrated analysis of aircraft and satellite observations. *Atmospheric Chemistry and Physics*, *10*(20), 9739–9760. https://doi.org/10.5194/acp-10-9739-2010

Andreae, M. O. (2019). Emission of trace gases and aerosols from biomass burning – An updated assessment. *Atmospheric Chemistry and Physics*, *19*(13), 8523–8546. https://doi.org/10.5194/acp-19-8523-2019

Angelbratt, J., Mellqvist, J., Simpson, D., Jonson, J. E., Blumenstock, T., Borsdorff, T., et al. (2011). Carbon monoxide (CO) and ethane (C_2H_6) trends from ground-based solar FTIR measurements at six European stations, comparison and sensitivity analysis with the EMEP model. *Atmospheric Chemistry and Physics*, *11*(17), 9253–9269. https://doi.org/10.5194/acp-11-9253-2011

Bader, W., Stavrakou, T., Muller, J.-F., Reimann, S., Boone, C. D., Harrison, J. J., et al. (2014). Long-term evolution and seasonal modulation of methanol above Jungfraujoch (46.5° N, 8.0° E): Optimisation of the retrieval strategy, comparison with model simulations and independent observations. *Atmospheric Measurement Techniques*, *7*(11), 3861–3872. https://doi.org/10.5194/amt-7-3861-2014

Batchelor, R. L., Strong, K., Lindenmaier, R., Mittermeier, R. L., Fast, H., Drummond, J. R., & Fogal, P. F. (2009). A new Bruker IFS 125HR FTIR spectrometer for the Polar Environment Atmospheric Research Laboratory at Eureka, Nunavut, Canada: Measurements and comparison with the existing Bomem DA8 spectrometer. *Journal of Atmospheric and Oceanic Technology*, *26*(7), 1328–1340. https://doi.org/10.1175/2009jtecha1215.1

Bates, K. H., Jacob, D. J., Wang, S., Hornbrook, R. S., Apel, E. C., Kim, M. J., et al. (2021). The global budget of atmospheric methanol: New constraints on secondary, oceanic, and terrestrial sources. *Journal of Geophysical Research: Atmospheres*, *126*(4), e2020JD033439. https://doi.org/10.1029/2020JD033439

Bernath, P., Steffen, J., Crouse, J., & Boone, C. (2020). Sixteen-year trends in atmospheric trace gases from orbit. *Journal of Quantitative Spectroscopy and Radiative Transfer*, *253*, 107178. https://doi.org/10.1016/j.jqsrt.2020.107178

Bridier, I., Caralp, F., Loirat, H., Lesclaux, R., Veyret, B., Becker, K. H., et al. (1991). Kinetic and theoretical studies of the reactions acetylperoxy + nitrogen dioxide + M ⇌ acetyl peroxynitrate + M between 248 and 393 K and between 30 and 760 Torr. *Journal of Physical Chemistry*, *95*(9), 3594–3600. https://doi.org/10.1021/j100162a031

Buchholz, R. R., Worden, H. M., Park, M., Francis, G., Deeter, M. N., Edwards, D. P., et al. (2021). Air Pollution Trends measured from Terra: CO and AOD over industrial, fire-prone, and background regions. *Remote Sensing of Environment*, *256*, 112275. https://doi.org/10.1016/j.rse.2020.112275

Cady-Pereira, K. E., Chaliyakunnel, S., Shephard, M. W., Millet, D. B., Luo, M., & Wells, K. C. (2014). HCOOH measurements from space: TES retrieval algorithm and observed global distribution. *Atmospheric Measurement Techniques*, *7*(7), 2297–2311. https://doi.org/10.5194/amt-7-2297-2014

Cady-Pereira, K. E., Shephard, M. W., Millet, D. B., Luo, M., Wells, K. C., Xiao, Y., et al. (2012). Methanol from TES global observations: Retrieval algorithm and seasonal and spatial variability. *Atmospheric Chemistry and Physics*, *12*(17), 8189–8203. https://doi.org/10.5194/acp-12-8189-2012

Chameides, W. L., & Davis, D. D. (1983). Aqueous-phase source of formic acid in clouds. *Nature*, *304*(5925), 427–429. https://doi.org/10.1038/304427a0

Chen, X., Millet, D. B., Neuman, J. A., Veres, P. R., Ray, E. A., Commane, R., et al. (2021). HCOOH in the remote atmosphere: Constraints from Atmospheric Tomography (ATom) airborne observations. *ACS Earth and Space Chemistry*, *5*(6), 1436–1454. https://doi.org/10.1021/acsearthspacechem.1c00049

Chen, X., Millet, D. B., Singh, H. B., Wisthaler, A., Apel, E. C., Atlas, E. L., et al. (2019). On the sources and sinks of atmospheric VOCs: An integrated analysis of recent aircraft campaigns over North America. *Atmospheric Chemistry and Physics*, *19*(14), 9097–9123. https://doi.org/10.5194/acp-19-9097-2019

Coheur, P.-F., Clarisse, L., Turquety, S., Hurtmans, D., & Clerbaux, C. (2009). IASI measurements of reactive trace species in biomass burning plumes. *Atmospheric Chemistry and Physics*, *9*(15), 5655–5667. https://doi.org/10.5194/acp-9-5655-2009

Cooper, O. R., Parrish, D. D., Stohl, A., Trainer, M., Nédélec, P., Thouret, V., et al. (2010). Increasing springtime ozone mixing ratios in the free troposphere over western North America. *Nature*, *463*(7279), 344–348. https://doi.org/10.1038/nature08708

Dalsøren, S. B., Myhre, G., Hodnebrog, O., Myhre, C. L., Stohl, A., Pisso, I., et al. (2018). Discrepancy between simulated and observed ethane and propane levels explained by underestimated fossil emissions. *Nature Geoscience*, *11*(3), 178–184. https://doi.org/10.1038/s41561-018-0073-0

Deeter, M. N., Emmons, L. K., Francis, G. L., Edwards, D. P., Gille, J. C., Warner, J. X., et al. (2003). Operational carbon monoxide retrieval algorithm and selected results for the MOPITT instrument. *Journal of Geophysical Research*, *108*(D14), 4399. https://doi.org/10.1029/2002jd003186

De Smedt, I., Stavrakou, T., Hendrick, F., Danckaert, T., Vlemmix, T., Pinardi, G., et al. (2015). Diurnal, seasonal and long-term variations of global formaldehyde columns inferred from combined OMI and GOME-2 observations. *Atmospheric Chemistry and Physics*, *15*(21), 12519–12545. https://doi.org/10.5194/acp-15-12519-2015

Dibb, J. E., & Arsenault, M. (2002). Shouldn't snowpacks be sources of monocarboxylic acids? *Atmospheric Environment*, *36*(15–16), 2513–2522. https://doi.org/10.1016/s1352-2310(02)00131-0

Duflot, V., Wespes, C., Clarisse, L., Hurtmans, D., Ngadi, Y., Jones, N., et al. (2015). Acetylene (C_2H_2) and hydrogen cyanide (HCN) from IASI satellite observations: Global Distributions, validation, and comparison with model. *Atmospheric Chemistry and Physics*, *15*(18), 10509–10527. https://doi.org/10.5194/acp-15-10509-2015

Eastham, S. D., Long, M. S., Keller, C. A., Lundgren, E., Yantosca, R. M., Zhuang, J., et al. (2018). GEOS-Chem High Performance (GCHP V11-02C): A next-generation implementation of the GEOS-chem chemical transport model for massively parallel applications. *Geoscientific Model Development*, *11*(7), 2941–2953. https://doi.org/10.5194/gmd-11-2941-2018

Fadnavis, S., Schultz, M. G., Semeniuk, K., Mahajan, A. S., Pozzoli, L., Sonbawne, S., et al. (2014). Trends in peroxyacetyl nitrate (PAN) in the upper troposphere and lower stratosphere over southern Asia during the summer monsoon season: Regional impacts. *Atmospheric Chemistry and Physics*, *14*(23), 12725–12743. https://doi.org/10.5194/acp-14-12725-2014

Fall, R., & Benson, A. A. (1996). Leaf methanol — The simplest natural product from plants. *Trends in Plant Science*, *1*(9), 296–301. https://doi.org/10.1016/s1360-1385(96)88175-0

Fischer, E. V., Jacob, D. J., Yantosca, R. M., Sulprizio, M. P., Millet, D. B., Mao, J., et al. (2014). Atmospheric peroxyacetyl nitrate (PAN): A global budget and source attribution. *Atmospheric Chemistry and Physics*, *14*(5), 2679–2698. https://doi.org/10.5194/acp-14-2679-2014

Fischer, E. V., Jaffe, D. A., & Weatherhead, E. C. (2011). Free tropospheric peroxyacetyl nitrate (PAN) and ozone at Mount Bachelor: Potential causes of variability and timescale for trend detection. *Atmospheric Chemistry and Physics*, *11*(12), 5641–5654. https://doi.org/10.5194/acp-11-5641-2011

Flannigan, M. D., Logan, K. A., Amiro, B. D., Skinner, W. R., & Stocks, B. J. (2005). Future area burned in Canada. *Climatic Change*, *72*(1–2), 1–16. https://doi.org/10.1007/s10584-005-5935-y

Folberth, G. A., Hauglustaine, D. A., Lathière, J., & Brocheton, F. (2006). Interactive chemistry in the Laboratoire de Météorologie Dynamique General Circulation Model: Model description and impact analysis of biogenic hydrocarbons on tropospheric chemistry. *Atmospheric Chemistry and Physics*, *6*(8), 2273–2319. https://doi.org/10.5194/acp-6-2273-2006

Franco, B., Bader, W., Toon, G., Bray, C., Perrin, A., Fischer, E., et al. (2015). Retrieval of ethane from ground-based FTIR solar spectra using improved spectroscopy: Recent burden increase above Jungfraujoch. *Journal of Quantitative Spectroscopy and Radiative Transfer*, *160*, 36–49. https://doi.org/10.1016/j.jqsrt.2015.03.017

Franco, B., Blumenstock, T., Cho, C., Clarisse, L., Clerbaux, C., Coheur, P.-F., et al. (2021). Ubiquitous atmospheric production of organic acids mediated by cloud droplets. *Nature*, *593*(7858), 233–237. https://doi.org/10.1038/s41586-021-03462-x

Franco, B., Mahieu, E., Emmons, L. K., Tzompa-Sosa, Z. A., Fischer, E. V., Sudo, K., et al. (2016a). Evaluating ethane and methane emissions associated with the development of oil and natural gas extraction in North America. *Environmental Research Letters*, *11*(4), 044010. https://doi.org/10.1088/1748-9326/11/4/044010

Franco, B., Marais, E. A., Bovy, B., Bader, W., Lejeune, B., Roland, G., et al. (2016b). Diurnal cycle and multi-decadal trend of formaldehyde in the remote atmosphere near 46°N. *Atmospheric Chemistry and Physics*, *16*(6), 4171–4189. https://doi.org/10.5194/acp-16-4171-2016

Friedrich, M., Beutner, E., Reuvers, H., Smeekes, S., Urbain, J.-P., Bader, W., et al. (2020). A statistical analysis of time trends in atmospheric ethane. *Climatic Change*, *162*(1), 105–125. https://doi.org/10.1007/s10584-020-02806-2

Fu, T.-M., Jacob, D. J., Palmer, P. I., Chance, K., Wang, Y. X., Barletta, B., et al. (2007). Space-based formaldehyde measurements as constraints on volatile organic compound emissions in east and South Asia and implications for ozone. *Journal of Geophysical Research*, *112*(D6), D06312. https://doi.org/10.1029/2006jd007853

Galloway, J. N., Likens, G. E., Keene, W. C., & Miller, J. M. (1982). The composition of precipitation in remote areas of the world. *Journal of Geophysical Research*, *87*(C11), 8771–8786. https://doi.org/10.1029/JC087iC11p08771

Gardiner, T., Forbes, A., De Mazière, M., Vigouroux, C., Mahieu, E., Demoulin, P., et al. (2008). Trend analysis of greenhouse gases over Europe measured by a network of ground-based remote FTIR instruments. *Atmospheric Chemistry and Physics*, *8*(22), 6719–6727. https://doi.org/10.5194/acp-8-6719-2008

Gatz, D. F., & Smith, L. (1995). The standard error of a weighted mean concentration—I. Bootstrapping vs other methods. *Atmospheric Environment*, *29*(11), 1185–1193. https://doi.org/10.1016/1352-2310(94)00210-c

Gelaro, R., McCarty, W., Suárez, M. J., Todling, R., Molod, A., Takacs, L., et al. (2017). The Modern-Era Retrospective Analysis for Research and Applications, Version 2 (MERRA-2). *Journal of Climate*, *30*(14), 5419–5454. https://doi.org/10.1175/jcli-d-16-0758.1

GEOS-Chem. (2023). GEOS-Chem High Performance (Version 14.1.0) [Software]. *Zenodo*. https://doi.org/10.5281/zenodo.7600586

Gordon, I., Rothman, L., Hill, C., Kochanov, R., Tan, Y., Bernath, P., et al. (2017). The HITRAN2016 molecular spectroscopic database. *Journal of Quantitative Spectroscopy and Radiative Transfer*, *203*, 3–69. https://doi.org/10.1016/j.jqsrt.2017.06.038

Guenther, A. B., Jiang, X., Heald, C. L., Sakulyanontvittaya, T., Duhl, T., Emmons, L. K., & Wang, X. (2012). The Model of Emissions of Gases and Aerosols from Nature Version 2.1 (MEGAN2.1): An extended and updated framework for modeling biogenic emissions. *Geoscientific Model Development*, *5*(6), 1471–1492. https://doi.org/10.5194/gmd-5-1471-2012

Hannigan, J. W., Coffey, M. T., & Goldman, A. (2009). Semiautonomous FTS observation system for remote sensing of stratospheric and tropospheric gases. *Journal of Atmospheric and Oceanic Technology*, *26*(9), 1814–1828. https://doi.org/10.1175/2009jtecha1230.1

Helmig, D., Rossabi, S., Hueber, J., Tans, P., Montzka, S. A., Masarie, K., et al. (2016). Reversal of global atmospheric ethane and propane trends largely due to US oil and natural gas production. *Nature Geoscience*, *9*(7), 490–495. https://doi.org/10.1038/ngeo2721

Hoesly, R. M., Smith, S. J., Feng, L., Klimont, Z., Janssens-Maenhout, G., Pitkanen, T., et al. (2018). Historical (1750–2014) anthropogenic emissions of reactive gases and aerosols from the Community Emissions Data System (CEDS). *Geoscientific Model Development*, *11*(1), 369–408. https://doi.org/10.5194/gmd-11-369-2018

Holloway, T., Levy, H., & Kasibhatla, P. (2000). Global distribution of carbon monoxide. *Journal of Geophysical Research*, *105*(D10), 12123–12147. https://doi.org/10.1029/1999jd901173

Holzinger, R., Warneke, C., Hansel, A., Jordan, A., Lindinger, W., Scharffe, D. H., et al. (1999). Biomass burning as a source of formaldehyde, acetaldehyde, methanol, acetone, acetonitrile, and hydrogen cyanide. *Geophysical Research Letters*, *26*(8), 1161–1164. https://doi.org/10.1029/1999gl900156

Jacob, D. (2000). Heterogeneous chemistry and tropospheric ozone. *Atmospheric Environment*, *34*(12–14), 2131–2159. https://doi.org/10.1016/s1352-2310(99)00462-8

Jiang, Z., Jones, D. B., Worden, J., Worden, H. M., Henze, D. K., & Wang, Y. X. (2015). Regional data assimilation of multi-spectral MOPITT observations of CO over North America. *Atmospheric Chemistry and Physics*, *15*(12), 6801–6814. https://doi.org/10.5194/acp-15-6801-2015

Jiang, Z., Worden, J. R., Payne, V. H., Zhu, L., Fischer, E., Walker, T., & Jones, D. B. (2016). Ozone export from East Asia: The role of PAN. *Journal of Geophysical Research: Atmospheres*, *121*(11), 6555–6563. https://doi.org/10.1002/2016jd024952

Juncosa Calahorrano, J. F., Lindaas, J., O'Dell, K., Palm, B. B., Peng, Q., Flocke, F., et al. (2020). Daytime oxidized reactive nitrogen partitioning in western U.S. wildfire smoke plumes. *Journal of Geophysical Research: Atmospheres*, *126*(4), e2020JD033484. https://doi.org/10.1029/2020jd033484

Kaiser, J. W., Heil, A., Andreae, M. O., Benedetti, A., Chubarova, N., Jones, L., et al. (2012). Biomass burning emissions estimated with a global fire assimilation system based on observed fire radiative power. *Biogeosciences*, *9*(1), 527–554. https://doi.org/10.5194/bg-9-527-2012

Kirchmeier-Young, M. C., Gillett, N. P., Zwiers, F. W., Cannon, A. J., & Anslow, F. S. (2019). Attribution of the influence of human-induced climate change on an extreme fire season. *Earth's Future*, *7*(1), 2–10. https://doi.org/10.1029/2018ef001050

Kopacz, M., Jacob, D. J., Fisher, J. A., Logan, J. A., Zhang, L., Megretskaia, I. A., et al. (2010). Global estimates of CO sources with high resolution by adjoint inversion of multiple satellite datasets (MOPITT, Airs, Sciamachy, TES). *Atmospheric Chemistry and Physics*, *10*(3), 855–876. https://doi.org/10.5194/acp-10-855-2010

Law, K. S., & Stohl, A. (2007). Arctic air pollution: Origins and impacts. *Science*, *315*(5818), 1537–1540. https://doi.org/10.1126/science.1137695

Law, K. S., Stohl, A., Quinn, P., Brock, C., Burkhart, J., Paris, J., et al. (2014). Arctic air pollution: New insights from POLARCAT-IPY. *Bulletin of the American Meteorological Society*, *95*(12), 1873–1895. https://doi.org/10.1175/bams-d-13-00017.1

Liang, Q., Rodriguez, J. M., Douglass, A. R., Crawford, J. H., Olson, J. R., Apel, E., et al. (2011). Reactive nitrogen, ozone and ozone production in the Arctic troposphere and the impact of stratosphere-troposphere exchange. *Atmospheric Chemistry and Physics*, *11*(24), 13181–13199. https://doi.org/10.5194/acp-11-13181-2011

Lin, H., Jacob, D. J., Lundgren, E. W., Sulprizio, M. P., Keller, C. A., Fritz, T. M., et al. (2021). Harmonized emissions component (HEMCO) 3.0 as a versatile emissions component for atmospheric models: Application in the GEOS-Chem, NASA GEOS, WRF-GC, CESM2, NOAA GEFS-aerosol, and NOAA UFS models. *Geoscientific Model Development*, *14*(9), 5487–5506. https://doi.org/10.5194/gmd-14-5487-2021

Liu, X., Zhang, Y., Huey, L. G., Yokelson, R. J., Wang, Y., Jimenez, J. L., et al. (2016). Agricultural fires in the South Eastern U.S. during SEAC4RS: Emissions of trace gases and particles and evolution of ozone, reactive nitrogen, and organic aerosol. *Journal of Geophysical Research: Atmospheres*, *121*(12), 7383–7414. https://doi.org/10.1002/2016jd025040

Luecken, D., Hutzell, W., Strum, M., & Pouliot, G. (2012). Regional sources of atmospheric formaldehyde and acetaldehyde, and implications for atmospheric modeling. *Atmospheric Environment*, *47*, 477–490. https://doi.org/10.1016/j.atmosenv.2011.10.005

Luecken, D., Napelenok, S. L., Strum, M., Scheffe, R., & Phillips, S. (2018). Sensitivity of ambient atmospheric formaldehyde and ozone to precursor species and source types across the United States. *Environmental Science & Technology*, *52*(8), 4668–4675. https://doi.org/10.1021/acs.est.7b05509

Lutsch, E., Dammers, E., Conway, S., & Strong, K. (2016). Long-range transport of NH_3, CO, HCN, and C_2H_6 from the 2014 Canadian wildfires. *Geophysical Research Letters*, *43*(15), 8286–8297. https://doi.org/10.1002/2016gl070114

Lutsch, E., Strong, K., Jones, D., Blumenstock, T., Conway, S., Fisher, J., et al. (2020). Detection and attribution of wildfire pollution in the Arctic and northern midlatitudes using a network of Fourier-transform infrared spectrometers and GEOS-Chem. *Atmospheric Chemistry and Physics*, *20*(21), 12813–12851. https://doi.org/10.5194/acp-20-12813-2020

Lutsch, E., Strong, K., Jones, D., Ortega, I., Hannigan, J., Dammers, E., et al. (2019). Unprecedented atmospheric ammonia concentrations detected in the high Arctic from the 2017 Canadian wildfires. *Journal of Geophysical Research: Atmospheres*, *124*(14), 8178–8202. https://doi.org/10.1029/2019jd030419

MacDonald, R. C., & Fall, R. (1993). Detection of substantial emissions of methanol from plants to the atmosphere. *Atmospheric Environment. Part A. General Topics*, *27*(11), 1709–1713. https://doi.org/10.1016/0960-1686(93)90233-o

Maddanu, F., & Proietti, T. (2023). Trends in atmospheric ethane. *Climatic Change*, *176*(5), 53. https://doi.org/10.1007/s10584-023-03508-1

Mahajan, A. S., Whalley, L. K., Kozlova, E., Oetjen, H., Mendez, L., Furneaux, K. L., et al. (2010). DOAS observations of formaldehyde and its impact on the HO_x balance in the tropical Atlantic marine boundary layer. *Journal of Atmospheric Chemistry*, *66*(3), 167–178. https://doi.org/10.1007/s10874-011-9200-7

Mahieu, E., Fischer, E. V., Franco, B., Palm, M., Wizenberg, T., Smale, D., et al. (2021). First retrievals of peroxyacetyl nitrate (PAN) from ground-based FTIR solar spectra recorded at remote sites, comparison with model and satellite data. *Elementa: Science of the Anthropocene*, *9*(1), 00027. https://doi.org/10.1525/elementa.2021.00027

Marelle, L., Thomas, J. L., Raut, J.-C., Law, K. S., Jalkanen, J.-P., Johansson, L., et al. (2016). Air quality and radiative impacts of Arctic shipping emissions in the summertime in Northern Norway: From the local to the regional scale. *Atmospheric Chemistry and Physics*, *16*(4), 2359–2379. https://doi.org/10.5194/acp-16-2359-2016

Marsh, D. R., Mills, M. J., Kinnison, D. E., Lamarque, J.-F., Calvo, N., & Polvani, L. M. (2013). Climate change from 1850 to 2005 simulated in CESM1 (WACCM). *Journal of Climate*, *26*(19), 7372–7391. https://doi.org/10.1175/jcli-d-12-00558.1

Martin, R. V., Eastham, S. D., Bindle, L., Lundgren, E. W., Clune, T. L., Keller, C. A., et al. (2022). Improved advection, resolution, performance, and community access in the new generation (version 13) of the high-performance GEOS-Chem global atmospheric chemistry model (GCHP). *Geoscientific Model Development*, *15*(23), 8731–8748. https://doi.org/10.5194/gmd-15-8731-2022

Monks, S. A., Wilson, C., Emmons, L. K., Hannigan, J. W., Helmig, D., Blake, N. J., & Blake, D. R. (2018). Using an inverse model to reconcile differences in simulated and observed global ethane concentrations and trends between 2008 and 2014. *Journal of Geophysical Research: Atmospheres*, *123*(19), 11262–11282. https://doi.org/10.1029/2017jd028112

Moxim, W. J., Levy, H., & Kasibhatla, P. S. (1996). Simulated global tropospheric PAN: Its transport and impact on NO_x. *Journal of Geophysical Research*, *101*(D7), 12621–12638. https://doi.org/10.1029/96jd00338

Mungall, E. L., Abbatt, J. P. D., Wentzell, J. J. B., Wentworth, G. R., Murphy, J. G., Kunkel, D., et al. (2018). High gas-phase mixing ratios of formic and acetic acid in the high Arctic. *Atmospheric Chemistry and Physics*, *18*(14), 10237–10254. https://doi.org/10.5194/acp-18-10237-2018

Notholt, J., Toon, G., Stordal, F., Solberg, S., Schmidbauer, N., Becker, E., et al. (1997). Seasonal variations of atmospheric trace gases in the high Arctic at 79°N. *Journal of Geophysical Research*, *102*(D11), 12855–12861. https://doi.org/10.1029/97JD00337

Notholt, J., Toon, G. C., Lehmann, R., Sen, B., & Blavier, J.-F. (1997). Comparison of Arctic and Antarctic trace gas column abundances from ground-based Fourier transform infrared spectrometry. *Journal of Geophysical Research*, *102*(D11), 12863–12869. https://doi.org/10.1029/97jd00358

Notholt, J., Toon, G. C., Rinsland, C. P., Pougatchev, N. S., Jones, N. B., Connor, B. J., et al. (2000). Latitudinal variations of trace gas concentrations in the free troposphere measured by solar absorption spectroscopy during a ship cruise. *Journal of Geophysical Research*, *105*(D1), 1337–1349. https://doi.org/10.1029/1999jd900940

Nussbaumer, C. M., Crowley, J. N., Schuladen, J., Williams, J., Hafermann, S., Reiffs, A., et al. (2021). Measurement report: Photochemical production and loss rates of formaldehyde and ozone across Europe. *Atmospheric Chemistry and Physics*, *21*(24), 18413–18432. https://doi.org/10.5194/acp-21-18413-2021

Orlando, J. J., Tyndall, G. S., & Calvert, J. G. (1992). Thermal decomposition pathways for peroxyacetyl nitrate (PAN): Implications for atmospheric methyl nitrate levels. *Atmospheric Environment. Part A. General Topics*, *26*(17), 3111–3118. https://doi.org/10.1016/0960-1686(92)90468-z

Paton-Walsh, C., Deutscher, N. M., Griffith, D. W., Forgan, B. W., Wilson, S. R., Jones, N. B., & Edwards, D. P. (2010). Trace gas emissions from savanna fires in northern Australia. *Journal of Geophysical Research*, *115*(D16), D16314. https://doi.org/10.1029/2009jd013309

Paton-Walsh, C., Jones, N. B., Wilson, S. R., Haverd, V., Meier, A., Griffith, D. W., & Rinsland, C. P. (2005). Measurements of trace gas emissions from Australian forest fires and correlations with coincident measurements of aerosol optical depth. *Journal of Geophysical Research*, *110*(D24), 2005JD006202. https://doi.org/10.1029/2005jd006202

Paulot, F., Wunch, D., Crounse, J. D., Toon, G. C., Millet, D. B., DeCarlo, P. F., et al. (2011). Importance of secondary sources in the atmospheric budgets of formic and acetic acids. *Atmospheric Chemistry and Physics*, *11*(5), 1989–2013. https://doi.org/10.5194/acp-11-1989-2011

Payne, V. H., Alvarado, M. J., Cady-Pereira, K. E., Worden, J. R., Kulawik, S. S., & Fischer, E. V. (2014). Satellite observations of peroxyacetyl nitrate from the AURA Tropospheric Emission Spectrometer. *Atmospheric Measurement Techniques*, *7*(11), 3737–3749. https://doi.org/10.5194/amt-7-3737-2014

Payne, V. H., Kulawik, S. S., Fischer, E. V., Brewer, J. F., Huey, L. G., Miyazaki, K., et al. (2022). Satellite measurements of peroxyacetyl nitrate from the Cross-Track Infrared Sounder: Comparison with ATom Aircraft Measurements. *Atmospheric Measurement Techniques*, *15*(11), 3497–3511. https://doi.org/10.5194/amt-15-3497-2022

Philip, S., Martin, R. V., & Keller, C. A. (2016). Sensitivity of chemistry-transport model simulations to the duration of chemical and transport operators: A case study with GEOS-chem V10-01. *Geoscientific Model Development*, *9*(5), 1683–1695. https://doi.org/10.5194/gmd-9-1683-2016

Pommier, M., Clerbaux, C., Coheur, P.-F., Mahieu, E., Müller, J.-F., Paton-Walsh, C., et al. (2016). HCOOH distributions from IASI for 2008–2014: Comparison with ground-based FTIR measurements and a global chemistry-transport model. *Atmospheric Chemistry and Physics*, *16*(14), 8963–8981. https://doi.org/10.5194/acp-16-8963-2016

Pougatchev, N. S., Connor, B. J., & Rinsland, C. P. (1995). Infrared measurements of the ozone vertical distribution above Kitt Peak. *Journal of Geophysical Research*, *100*(D8), 16689–16697. https://doi.org/10.1029/95JD01296

Razavi, A., Karagulian, F., Clarisse, L., Hurtmans, D., Coheur, P. F., Clerbaux, C., et al. (2011). Global distributions of methanol and formic acid retrieved for the first time from the IASI/MetOp Thermal Infrared Sounder. *Atmospheric Chemistry and Physics*, *11*(2), 857–872. https://doi.org/10.5194/acp-11-857-2011

Rodgers, C. D. (2000). *Inverse methods for atmospheric sounding: Theory and practice*. World Scientific.

Roiger, A., Schlager, H., Schäfler, A., Huntrieser, H., Scheibe, M., Aufmhoff, H., et al. (2011). In-situ observation of Asian pollution transported into the Arctic lowermost stratosphere. *Atmospheric Chemistry and Physics*, *11*(21), 10975–10994. https://doi.org/10.5194/acp-11-10975-2011

Roiger, A., Thomas, J.-L., Schlager, H., Law, K. S., Kim, J., Schäfler, A., et al. (2015). Quantifying emerging local anthropogenic emissions in the Arctic region: The ACCESS Aircraft Campaign Experiment. *Bulletin of the American Meteorological Society*, *96*(3), 441–460. https://doi.org/10.1175/bams-d-13-00169.1

Rothman, L. S., Gordon, I. E., Barbe, A., Benner, D., Bernath, P. F., Birk, M., et al. (2009). The HITRAN 2008 molecular spectroscopic database. *Journal of Quantitative Spectroscopy and Radiative Transfer*, *110*(9–10), 533–572. https://doi.org/10.1016/j.jqsrt.2009.02.013

Schobesberger, S., Lopez-Hilfiker, F. D., Taipale, D., Millet, D. B., D'Ambro, E. L., Rantala, P., et al. (2016). High upward fluxes of formic acid from a boreal forest canopy. *Geophysical Research Letters*, *43*(17), 9342–9351. https://doi.org/10.1002/2016gl069599

Shindell, D. T., Chin, M., Dentener, F., Doherty, R. M., Faluvegi, G., Fiore, A. M., et al. (2008). A multi-model assessment of pollution transport to the Arctic. *Atmospheric Chemistry and Physics*, *8*(17), 5353–5372. https://doi.org/10.5194/acp-8-5353-2008

Shindell, D. T., & Faluvegi, G. (2009). Climate response to regional radiative forcing during the twentieth century. *Nature Geoscience*, *2*(4), 294–300. https://doi.org/10.1038/ngeo473

Shindell, D. T., Faluvegi, G., Stevenson, D. S., Krol, M. C., Emmons, L. K., Lamarque, J., et al. (2006). Multimodel simulations of carbon monoxide: Comparison with observations and projected near-future changes. *Journal of Geophysical Research*, *111*(D19), 2006JD007100. https://doi.org/10.1029/2006jd007100

Shogrin, M. J., Payne, V. H., Kulawik, S. S., Miyazaki, K., & Fischer, E. V. (2023). Measurement report: Spatiotemporal variability of peroxy acyl nitrates (PANs) over Mexico City from TES and CrIS satellite measurements. *Atmospheric Chemistry and Physics*, *23*(4), 2667–2682. https://doi.org/10.5194/acp-23-2667-2023

Singh, H. B., Herlth, D., O'Hara, D., Zahnle, K., Bradshaw, J. D., Sandholm, S. T., et al. (1992). Relationship of peroxyacetyl nitrate to active and total odd nitrogen at northern high latitudes: Influence of reservoir species on NO_x and O_3. *Journal of Geophysical Research*, *97*(D15), 16523–16530. https://doi.org/10.1029/91jd00890

Stavrakou, T., Guenther, A., Razavi, A., Clarisse, L., Clerbaux, C., Coheur, P.-F., et al. (2011). First space-based derivation of the global atmospheric methanol emission fluxes. *Atmospheric Chemistry and Physics*, *11*(10), 4873–4898. https://doi.org/10.5194/acp-11-4873-2011

Stavrakou, T., Müller, J.-F., Peeters, J., Razavi, A., Clarisse, L., Clerbaux, C., et al. (2012). Satellite evidence for a large source of formic acid from boreal and tropical forests. *Nature Geoscience*, *5*(1), 26–30. https://doi.org/10.1038/ngeo1354

Stohl, A. (2006). Characteristics of atmospheric transport into the Arctic troposphere. *Journal of Geophysical Research*, *111*(D11), 2005JD006888. https://doi.org/10.1029/2005JD006888

Stohl, A., Klimont, Z., Eckhardt, S., Kupiainen, K., Shevchenko, V. P., Kopeikin, V. M., & Novigatsky, A. N. (2013). Black Carbon in the Arctic: The underestimated role of gas flaring and residential combustion emissions. *Atmospheric Chemistry and Physics*, *13*(17), 8833–8855. https://doi.org/10.5194/acp-13-8833-2013

Talukdar, R. K., Burkholder, J. B., Schmoltner, A.-M., Roberts, J. M., Wilson, R. R., & Ravishankara, A. R. (1995). Investigation of the loss processes for peroxyacetyl nitrate in the atmosphere: UV photolysis and reaction with OH. *Journal of Geophysical Research*, *100*(D7), 14163–14173. https://doi.org/10.1029/95jd00545

Tie, X., Guenther, A., & Holland, E. (2003). Biogenic methanol and its impacts on tropospheric oxidants. *Geophysical Research Letters*, *30*(17), 1881. https://doi.org/10.1029/2003gl017167

Toon, G. C., Blavier, J.-F., Sung, K., Rothman, L. S., & E. Gordon, I. (2016). HITRAN spectroscopy evaluation using solar occultation FTIR spectra. *Journal of Quantitative Spectroscopy and Radiative Transfer*, *182*, 324–336. https://doi.org/10.1016/j.jqsrt.2016.05.021

Tzompa-Sosa, Z. A., Mahieu, E., Franco, B., Keller, C. A., Turner, A. J., Helmig, D., et al. (2017). Revisiting global fossil fuel and biofuel emissions of ethane. *Journal of Geophysical Research: Atmospheres*, *122*(4), 2493–2512. https://doi.org/10.1002/2016jd025767

Van Der Werf, G. R., Randerson, J. T., Giglio, L., Van Leeuwen, T. T., Chen, Y., Rogers, B. M., et al. (2017). Global fire emissions estimates during 1997–2016. *Earth System Science Data*, *9*(2), 697–720. https://doi.org/10.5194/essd-9-697-2017

Viatte, C., Strong, K., Hannigan, J., Nussbaumer, E., Emmons, L. K., Conway, S., et al. (2015). Identifying fire plumes in the Arctic with tropospheric FTIR measurements and transport models. *Atmospheric Chemistry and Physics*, *15*(5), 2227–2246. https://doi.org/10.5194/acp-15-2227-2015

Viatte, C., Strong, K., Paton-Walsh, C., Mendonca, J., O'Neill, N. T., & Drummond, J. R. (2013). Measurements of CO, HCN, and C_2H_6 total columns in smoke plumes transported from the 2010 Russian boreal forest fires to the Canadian high Arctic. *Atmosphere-Ocean*, *51*(5), 522–531. https://doi.org/10.1080/07055900.2013.823373

Viatte, C., Strong, K., Walker, K. A., & Drummond, J. R. (2014). Five years of CO, HCN, C_2H_6, C_2H_2, CH_3OH, HCOOH, and H_2CO total columns measured in the Canadian high Arctic. *Atmospheric Measurement Techniques*, *7*(6), 1547–1570. https://doi.org/10.5194/amt-7-1547-2014

Vigouroux, C., Bauer Aquino, C. A., Bauwens, M., Becker, C., Blumenstock, T., De Mazière, M., et al. (2018). NDACC harmonized formaldehyde time series from 21 FTIR stations covering a wide range of column abundances. *Atmospheric Measurement Techniques*, *11*(9), 5049–5073. https://doi.org/10.5194/amt-11-5049-2018

Vigouroux, C., Langerock, B., Aquino, C. A. B., Blumenstock, T., Cheng, Z., Mazière, M. D., et al. (2020). TROPOMI–Sentinel-5 Precursor formaldehyde validation using an extensive network of ground-based Fourier-transform infrared stations. *Atmospheric Measurement Techniques*, *13*(7), 3751–3767. https://doi.org/10.5194/amt-13-3751-2020

Vigouroux, C., Stavrakou, T., Whaley, C., Dils, B., Duflot, V., Hermans, C., et al. (2012). FTIR time-series of biomass burning products (HCN, C_2H_6, C_2H_2, CH_3OH, and HCOOH) at Reunion Island (21° S, 55° E) and comparisons with model Data. *Atmospheric Chemistry and Physics*, *12*(21), 10367–10385. https://doi.org/10.5194/acp-12-10367-2012

Wells, K. C., Millet, D. B., Cady-Pereira, K. E., Shephard, M. W., Henze, D. K., Bousserez, N., et al. (2014). Quantifying global terrestrial methanol emissions using observations from the TES satellite sensor. *Atmospheric Chemistry and Physics*, *14*(5), 2555–2570. https://doi.org/10.5194/acp-14-2555-2014

Whaley, C. H., Mahmood, R., Von Salzen, K., Winter, B., Eckhardt, S., Arnold, S., et al. (2022). Model evaluation of short-lived climate forcers for the Arctic Monitoring and Assessment Programme: A multi-species, multi-model study. *Atmospheric Chemistry and Physics*, *22*(9), 5775–5828. https://doi.org/10.5194/acp-22-5775-2022

Wittrock, F., Richter, A., Oetjen, H., Burrows, J. P., Kanakidou, M., Myriokefalitakis, S., et al. (2006). Simultaneous global observations of glyoxal and formaldehyde from space. *Geophysical Research Letters*, *33*(16), L16804. https://doi.org/10.1029/2006gl026310

Wizenberg, T., Strong, K., Jones, D. B., Lutsch, E., Mahieu, E., Franco, B., & Clarisse, L. (2023). Exceptional wildfire enhancements of PAN, C_2H_4, CH_3OH, and HCOOH over the Canadian high Arctic during August 2017. *Journal of Geophysical Research: Atmospheres*, *128*(10), e2022JD038052. https://doi.org/10.1029/2022jd038052

Wizenberg, T., Strong, K., Jones, D. B. A., Hannigan, J. W., Ortega, I., & Mahieu, E. (2023). Replication data for: Measured and modeled trends of seven tropospheric pollutants in the high Arctic from 1999–2022. *Borealis*. https://doi.org/10.5683/SP3/CSGZBA

Wofsy, S. C., Sachse, G. W., Gregory, G. L., Blake, D. R., Bradshaw, J. D., Sandholm, S. T., et al. (1992). Atmospheric chemistry in the Arctic and subarctic: Influence of natural fires, industrial emissions, and stratospheric inputs. *Journal of Geophysical Research*, *97*(D15), 16731–16746. https://doi.org/10.1029/92jd00622

Wohl, C., Jones, A. E., Sturges, W. T., Nightingale, P. D., Else, B., Butterworth, B. J., & Yang, M. (2022). Sea ice concentration impacts dissolved organic gases in the Canadian Arctic. *Biogeosciences*, *19*(4), 1021–1045. https://doi.org/10.5194/bg-19-1021-2022

Worden, H. M., Deeter, M. N., Frankenberg, C., George, M., Nichitiu, F., Worden, J., et al. (2013). Decadal record of satellite carbon monoxide observations. *Atmospheric Chemistry and Physics*, *13*(2), 837–850. https://doi.org/10.5194/acp-13-837-2013

Xiao, Y., Jacob, D. J., & Turquety, S. (2007). Atmospheric acetylene and its relationship with CO as an indicator of air mass age. *Journal of Geophysical Research*, *112*(D12), 2006JD008268. https://doi.org/10.1029/2006jd008268

Xiao, Y., Logan, J. A., Jacob, D. J., Hudman, R. C., Yantosca, R., & Blake, D. R. (2008). Global budget of ethane and regional constraints on U.S. sources. *Journal of Geophysical Research*, *113*(D21), 2007JD009415. https://doi.org/10.1029/2007jd009415

Yamanouchi, S., Strong, K., Colebatch, O., Conway, S., Jones, D. B., Lutsch, E., & Roche, S. (2021). Atmospheric Trace gas trends obtained from FTIR column measurements in Toronto, Canada from 2002-2019. *Environmental Research Communications*, *3*(5), 051002. https://doi.org/10.1088/2515-7620/abfa65

Yamanouchi, S., Strong, K., Lutsch, E., & Jones, D. B. (2020). Detection of HCOOH, CH_3OH, CO, HCN, and C_2H_6 in wildfire plumes transported over Toronto using ground-based FTIR measurements from 2002–2018. *Journal of Geophysical Research: Atmospheres*, *125*(16), e2019JD031924. https://doi.org/10.1029/2019jd031924

Yang, H., Waugh, D. W., Orbe, C., & Chen, G. (2020). Dependence of atmospheric transport into the Arctic on the meridional extent of the Hadley Cell. *Geophysical Research Letters*, *47*(20), e2020GL090133. https://doi.org/10.1029/2020gl090133

Yang, M., Nightingale, P. D., Beale, R., Liss, P. S., Blomquist, B., & Fairall, C. (2013). Atmospheric deposition of methanol over the Atlantic Ocean. *Proceedings of the National Academy of Sciences*, *110*(50), 20034–20039. https://doi.org/10.1073/pnas.1317840110

Yu, K., Keller, C. A., Jacob, D. J., Molod, A. M., Eastham, S. D., & Long, M. S. (2018). Errors and improvements in the use of archived meteorological data for chemical transport modeling: An analysis using GEOS-Chem V11-01 driven by GEOS-5 meteorology. *Geoscientific Model Development*, *11*(1), 305–319. https://doi.org/10.5194/gmd-11-305-2018

Yurganov, L., Grechko, E., & Dzhola, A. (1995). Carbon monoxide and total ozone in Arctic and Antarctic regions: Seasonal variations, long-term trends and relationships. *Science of the Total Environment*, *160–161*, 831–840. https://doi.org/10.1016/0048-9697(95)04416-x

Zander, R., Duchatelet, P., Mahieu, E., Demoulin, P., Roland, G., Servais, C., et al. (2010). Formic acid above the Jungfraujoch during 1985–2007: Observed variability, seasonality, but no long-term background evolution. *Atmospheric Chemistry and Physics*, *10*(20), 10047–10065. https://doi.org/10.5194/acp-10-10047-2010

Zellweger, C., Hüglin, C., Klausen, J., Steinbacher, M., Vollmer, M., & Buchmann, B. (2009). Inter-comparison of four different carbon monoxide measurement techniques and evaluation of the long-term carbon monoxide time series of Jungfraujoch. *Atmospheric Chemistry and Physics*, *9*(11), 3491–3503. https://doi.org/10.5194/acp-9-3491-2009

Zhang, L., Jacob, D. J., Boersma, K. F., Jaffe, D. A., Olson, J. R., Bowman, K. W., et al. (2008). Transpacific transport of ozone pollution and the effect of recent Asian emission increases on air quality in North America: An integrated analysis using satellite, aircraft, ozonesonde, and surface observations. *Atmospheric Chemistry and Physics*, *8*(20), 6117–6136. https://doi.org/10.5194/acp-8-6117-2008

Zhang, X., Liu, J., Han, H., Zhang, Y., Jiang, Z., Wang, H., et al. (2020). Satellite-observed variations and trends in carbon monoxide over Asia and their sensitivities to biomass burning. *Remote Sensing*, *12*(5), 830. https://doi.org/10.3390/rs12050830

Zhao, T., Mao, J., Simpson, W. R., De Smedt, I., Zhu, L., Hanisco, T. F., et al. (2022). Source and variability of formaldehyde (HCHO) at northern high latitudes: An integrated satellite, aircraft, and model study. *Atmospheric Chemistry and Physics*, *22*(11), 7163–7178. https://doi.org/10.5194/acp-22-7163-2022

Zhao, Y., Strong, K., Kondo, Y., Koike, M., Matsumi, Y., Irie, H., et al. (2002). Spectroscopic measurements of tropospheric CO, C_2H_6, C_2H_2, and HCN in northern Japan. *Journal of Geophysical Research*, *107*(D18), ACH2-1–ACH2-16. https://doi.org/10.1029/2001JD000748